IRRADIATION STABILITY OF CARBON NANOTUBES

A Thesis

by

ASSEL AITKALIYEVA

Submitted to the Office of Graduate Studies of
Texas A&M University
in partial fulfillment of the requirements for the degree of

MASTER OF SCIENCE

August 2009

Major Subject: Nuclear Engineering

IRRADIATION STABILITY OF CARBON NANOTUBES

A Thesis

by

ASSEL AITKALIYEVA

Submitted to the Office of Graduate Studies of
Texas A&M University
in partial fulfillment of the requirements for the degree of

MASTER OF SCIENCE

Approved by:

Chair of Committee,	Lin Shao
Committee Members,	Sean McDeavitt
	Xinghang Zhang
Head of Department,	Raymond Juzaitis

August 2009

Major Subject: Nuclear Engineering

ABSTRACT

Irradiation Stability of Carbon Nanotubes. (August 2009)

Assel Aitkaliyeva, B.S., al-Farabi Kazakh State University

Chair of Advisory Committee: Dr. Lin Shao

Ion irradiation of carbon nanotubes is a tool that can be used to achieve modification of the structure. Irradiation stability of carbon nanotubes was studied by ion and electron bombardment of the samples. Different ion species at various energies were used in experiments, and several defect characterization techniques were applied to characterize the damage.

Development of dimensional changes of carbon nanotubes in microscopes operated at accelerating voltages of 30 keV revealed that binding energy of carbon atoms in CNs is much lower than in bulk materials. Resistivity measurements during irradiation demonstrated existence of a quasi state of defect creation. Linear relationship between I_D/I_G ratio and increasing irradiation fluence was revealed by Raman spectroscopy study of irradiated carbon buckypapers. The deviations from linear relationship were observed for the samples irradiated to very high fluence values. Annealing of irradiated samples was able to reduce the value of I_D/I_G ratio and remove defects. However, annealing could not affect I_D/I_G ratio and remove defects in amorphized samples. The extracted value of activation energy for irradiated sample was 0.36 ±0.05 eV. The value of activation energy was in good agreement with theoretical studies.

DEDICATION

To my family, who always supported and encouraged me.

ACKNOWLEDGEMENTS

I would like to acknowledge Dr. Lin Shao without whom this thesis would not have been possible. His supervision, advice, guidance, as well as encouragement and support were invaluable for me.

I would like to thank my committee members, Dr. Sean McDeavitt and Dr. Xinghang Zhang for their help and support throughout the course of this research.

I express a special gratitude to Michael Colin McCarthy and Michael Martin who spent countless hours helping me with experiments and characterization of the samples. I want to express my gratitude to my team members Jesse Carter and Mark Hollander for helping in understanding of accelerator system. I also gratefully acknowledge our collaborators Dr. Hae-Kwon Jeong, Dr. Luohan Peng, Dr. Xuemei Wang, Dr. Wei-Kan Chu, Engang Fu, and Dharshana Wijesundera.

Finally, I am grateful to my family to whom I owe everything in my life, and to my dear friend Dinmukhamed Sunnatov who helped me through these years.

NOMENCLATURE

A	Ampere
AC	Alternating Current
Au	Gold
C	Carbon
CBP	Carbon Buckypaper
cm	Centimeter
CN	Carbon Nanotube
CVD	Chemical Vapor Deposition
DC	Direct Current
DI	De-Ionized
DPA	Displacement per Atom
eV	Electron Volt
FIB	Focused Ion Beam
H	Hydrogen
He	Helium
InGaAs	Indium-Gallium-Arsenide
LMIS	Liquid Metal Ion Source
K	Kelvin
keV	Kilo Electron Volt
kV	Kilo Volt

MeV	Mega Electron Volt
MD	Molecular Dynamics
Min	Minute
MWNT	Multi-Walled Carbon Nanotube
mm	Millimeter
nm	Nanometer
pA	Pico Ampere
PECVD	Plasma Enhanced Chemical Vapor Deposition
PKA	Primary Knock-On Atom
PPM	Parts per Million
RF	Radiofrequency
Sec	Second
SDS	Sodium Dedocyl Sulfate
SE	Secondary Electron
SEM	Scanning Electron Microscope
SRIM	Stopping and Range of Ion in Matter
SW	Stone-Wales
SWNT	Single-Walled Carbon Nanotube
TEM	Transmission Electron Microscope
TBMD	Tight-Binding Molecular Dynamics
um	Micrometer
V	Volt
Xe	Xenon

TABLE OF CONTENTS

LIST OF FIGURES

FIGURE   Page

CHAPTER I

INTRODUCTION

Since their discovery by Iijima in 1991, carbon nanotubes (CNs) evolved into independent research field [1]. Theoretical and experimental studies on properties of carbon nanotubes proved that they have unique properties such as thermal, mechanical and electronic transport [1-6]. Carbon nanotubes can be employed in fabrication of nonvolatile memory elements – molecular microswitches, advanced sensors and detectors, high strength and thermal conductivity materials, and shielding materials for neutron sources [5-13].

Driven by desire to fabricate a low cost and highly efficient doping method for controlling electronic properties of CNs, ion irradiation of nanotubes was found to be very a promising tool in achieving modification of a nanosystem in selected areas with high repeatability and uniformity. Irradiation is extensively used in semiconductor industry as a method of modifying the properties of materials in a controllable way. As it has been shown previously, irradiation can affect CNs in following ways: a) it is able to induce high pressure inside of nanotubes which results in phase changes, b) can form stable covalent links between neighboring tubes thus giving rise to enhancement of shear modulus by inter-tube bridging, c) can cut CNs, d) can transform bundle of SWNTs into a MWNT, and e) is able to bend the tubes and adjust their diameters [11-17].

_____

This thesis follows the style of Nuclear Instruments & Methods in Physics Research B.

As a result of irradiation, formation of unique pentagon/heptagon Stone-Wales defects can occur in nanotubes. The structure and size of CNs are responsible for preferable saturation of unfavorable dangling bonds. Recent studies reported reconstruction of vacancies, di-vacancies, and multi-vacancies, and self diffusion mechanism in MWNTs through vacancy holes/tubes. At this point much less is known about reconstruction of atoms in the neighborhood of interstitials, which are considered to be highly mobile in MWNTs. The possibility of interstitial-vacancy recombination in MWNTs remains unknown.

Despite the fact that defects in fission reactor material – graphite have been studied since 1950s, defect annealing and agglomeration in the material still lacks a comprehensive microscopic picture [17]. Recent experimental [18-19], and theoretical [20-23] studies revealed misapprehension of previous results [24] such as migration energies of point defects. It is believed that simpler, one dimensional structure of carbon nanotubes will be able to facilitate understanding the constitution of defects in graphite [17].

Regardless of all the work conducted on investigating the effects of irradiation on CNs, and CNs based materials, radiation damage in CNs is still deficient in fundamental understanding. In order to use carbon nanotubes in various fields, irradiation response and stability of CNs should be studied thoroughly.

The aim of this thesis is to study irradiation stability of carbon nanotubes. Since damage morphology is peculiar for various ion species, irradiation of carbon nanotubes with several ion species is required to investigate ability of CNs to repair damage

produced upon irradiation. Different ion species at various energies were chosen to bombard vertically aligned carbon nanotubes and carbon buckypapers. Irradiation to different fluence values, fluxes, temperatures, and post irradiation annealing experiments were able to extract activation energy which can be interpreted as interstitial and vacancy migration energies, or the energy barrier for defect recombination. Different types of defect characterization techniques were used to discriminate the damage formation mechanism in carbon nanotubes. Stability of vertically aligned carbon nanotubes in microscopes under electron and ion beams was studied. In situ resistivity measurements during irradiation revealed the dynamic defect recombination and a role of the surface in defect annealing. Raman spectroscopy study was able to extract activation energy for defect annealing in irradiated CNs.

CHAPTER II

EXPERIMENTAL SYSTEM

2.1. Ion Acceleration System

The experiments were done in the University of Houston and Texas A&M Ion Beam Lab using 2 MeV and 150 keV linear accelerators, respectively. Figure 1 corresponds to the description of 150 keV acceleration system used in experiments. The types of ions used in the experiments were singly charged hydrogen and helium atoms of 99.9% purity which were fed into a Physicon hot cathode ion source.

Protons resulted from collisions between electrons emitted from tungsten filament and the hydrogen atoms, are forced into the acceleration column and exposed to an electric potential of 150 keV. To minimize proton-gas collisions and sustain same energy of protons in the beam, a high vacuum should be established in the system. In compliance with the electric potential equation ($E=qV$) charged atom should be accelerated and leave with a beam energy of ~150 keV. The energy spread of beam protons leaving the source was ~30 eV, and since the value is smaller than the proton energy beam was considered as monoenergetic.

Reducing the beam size to the millimeter range involves a set of focusing lens electrodes. Beam current was adjusted by focusing and spreading the beam to assure that desired current of protons has been dispatched through a collimator. Once protons pass through the accelerating column, they are introduced into a glass cross region where the beam can be modified. A glass cross region includes a shutter to stop the beam and

measure the beam current, a set of vertical deflection plates that adjust the height of the

beam, and is connected to the 6-inch Varian diffusion pump maintaining the pressure of

~8x10^{-7} Torr. In order to ensure that only a certain type of ions, in this case hydrogen or

helium have a trajectory leading to the collisions with the target, magnetic field was

generated by the separation magnet. Typical magnetic fields in the given region were in

the range of 0.01-0.1 Tesla, varying with the mass and energy of ions.

A Physicon Ion Source
B Acceleration Column
C Electron Backstreaming Barrier
D Vertical and Horizontal Deflection Plate Assembly
E Glass Cross Shutter
F Glass Cross
G Diffusion Pump
H Separator Magnet

I First Collimator
J Sweep Plates
K Ion Pump
L Horizontal and Vertical Collimators
M Liquid Nitrogen Cold Trap
N Beam Profile Monitor
O Target Chamber Collimator
P Target Chamber

Fig. 1. Schematics of accelerator system [25].

Ion beam leaving a glass cross region enters the beam line maintained at the

pressure of 10^{-8} Torr to minimize the gas collisions. The final beam can be shaped by the

use of a collimator located in front of the target chamber and set to a diameter of 5/8 inch in the present experiment. Nitrogen cold trap located at the end of the beam line was used to trap substances such as pump oil to keep the target chamber clean. The pressure of the target chamber was sustained at 10^{-8} Torr during operations with well-baffled diffusion and cryogenic pumps. Electrons from the walls and collimators which might collate the proton beam are repelled by the negatively biased cup (constant at -200 V) in the opening of the target chamber.

A shutter attached to the electrometer inside the target chamber can block the beam to measure the electrical current and can unblock it to allow the beam flow into the chamber. The shutter is adjacent with the negatively biased cup and repels secondary electrons thus providing precise measurements of the beam current. Beam travels through the center of the large 70% transmission ion suppression grid which plane is perpendicular to the beam direction. A mesh through which the beam passes is located in the center of the grid and can be positively or negatively charged to suppress secondary electrons produced in the chamber wall that can affect collection efficiency. The mesh is connected to the battery box outside the chamber so that its bias can be varied from 0 to 540 V in 90 V increments [26].

Resistivity measurements were provided by a two-point probe technique during ion irradiation using a nanovolt amplifier and a digital voltmeter with a sensitivity corresponding to a resistivity of 10^{-11} Ω-cm. For semiconductors two-point probe set up gives better spatial resolution that four-point probe technique, and multi walled carbon nanotubes used in experiments were semiconducting. Current and voltage were read into

a computer via Matlab program. One of the point probes carried current while the other one sensed the voltage. Considering the value of the changes in resistivity of CNs produced by a vacancy (10^{-4} Ω-cm), the detection limitation of the approach was estimated to be around 0.1 parts per million (ppm) defect concentration. Contacts were fabricated with gold (Au) using standard photolithographic and thin film techniques. Two wires were brought into a contact with the surface. The current between probes expands over a small area, and is known as spreading resistance. In order not to damage the contacts, area exposed to the beam was limited by the region between two contacts such that they were not exposed to the beam.

2.2. Raman Spectrometer

The Raman spectra were acquired by using Horiba Jobin-Yvon LabRam Microscope in the Materials Characterization Facility of Texas A&M University. The typical Raman instrumentation consists of laser, Rayleigh filter, lenses, spectrograph and a detector. Refer to Fig. 2 during the description of the microscope. In a typical arrangement of the microscope the laser is focused through a pinhole, and to fill the optics of the microscope is congregated as an expanded beam. Any background radiation from the laser or emission from lines other than main exciting line of the laser is removed by a plasma filter. Once the laser radiation contacts the filter, it is reflected to the microscope through the optics, and then is passed into the monocromator and detector [27].
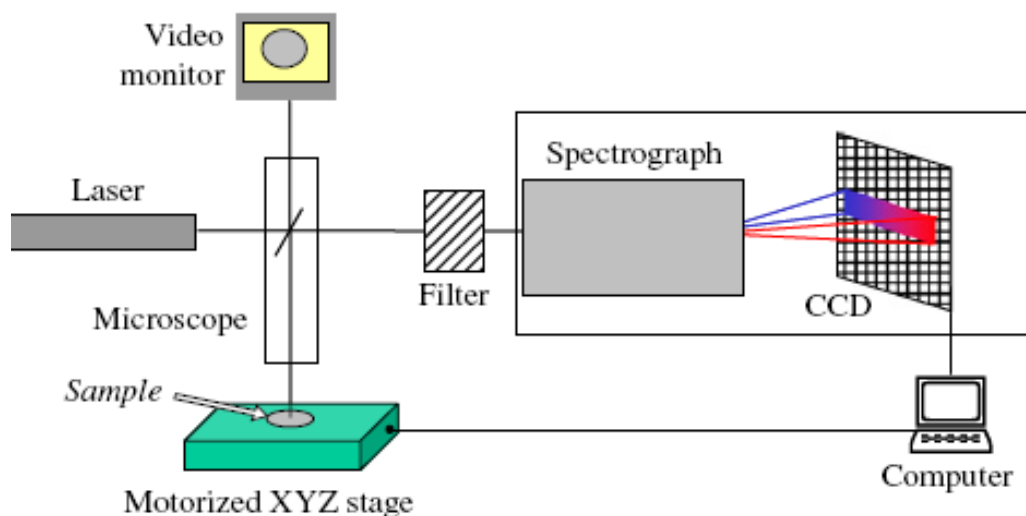
Fig. 2. Working principle of Raman spectrometer [28].

The system used in experiment combines Raman and FTIR microspectroscopy, and offers automated three directional mapping. The microscope installed in the system is Olympus BX 41. A stigmatic 800 nm spectrograph with two confocal spectrometer entrances is build into the system. One of the spectrometer entrances is connected to the microscope while the other one is connected by a fibre optics coupler. The system includes two sets of detectors which should be used depending on the spectral range of operation mode. The Jobin-Yvon open electrode CCD detector with enhanced quantum efficiency is used in the spectral range between 450-950 nm, and indium-gallium-arsenide (InGaAs) diode array JY IGA-3000 is preferred in the range between 900-1700 nm.

A 17 mW Class 3B He-Ne laser was used for excitation at a wavelength of 633 nm. The laser source provides high beam quality, high stability, extended lifetime,

and reliability. The properly chosen laser wavelength is of great importance, since for fluorescent species usage of the laser with excitation wavelength of 532 nm can cause fluorescence such that underlying Raman spectrum will not be detectable. With decreasing photon energy, in case of the lasers with the wavelengths of 633 and 785 nm, the probability of fluorescence decreases, and Raman scattering will be detected. However, with increasing wavelength, scattering efficiency starts decreasing, acquiring longer integration times or usage of higher laser powers. Filter was used to reduce the power of the laser hitting the sample thus minimizing the damage created by laser itself. The spectral resolution was around 1 cm^{-1}. The imaging resolution was diffraction limited. The spectra were fitted with a nanonics imaging Raman module, and analyzed with NGS LabSpec (ver. 5.23.24) software by decomposing into individual Lorentzian-shaped bands with a least-squares algorithm.

2.3. Annealing System

Annealing of the samples was performed in a vacuum furnace in the Texas A&M Ion Beam Lab. The high temperature tube furnace has silicon carbide heating elements which are fixed below and above the heated chamber. Temperature uniformity is achieved by graded layers of insulation and insulation vestibules. The heating was controlled by Lindberg temperature controller and the cooling depends on heat dissipation, so that it was slow in a vacuum. The temperature values were recorded using a separate thermocouple to ensure precise temperature reading. The vacuum pressure was monitored using ionization gauge and its value was better than 1×10^{-6} Torr.

The annealing used a "hot zone" approach in which the sample was quickly pushed into the hot zone once set up at desired annealing temperature. After annealing for chosen interval of time, the sample was quickly extracted out of the hot zone region and cooled down in a vacuum. The annealing periods were elected to be of 15 minutes for all annealing temperatures.

2.4. Scanning Electron Microscope

The secondary electron images were acquired using JEOL JSM-6400 microscope at the Microscopy and Imaging center of Texas A&M University and FEI Strata^{TM} DB 235 SEM/FIB microscope at the Nano Fabrication and Characterization Facility of the University of Texas at Austin.

Figure 3 shows schematics of a typical scanning electron microscope. Once electron beam is emitted from an electron gun, is focused by condenser lenses, and passes though deflection coils that scan the beam in a raster way over a rectangular area. The thermionic electron gun generates electron cloud by heating the filament to high temperatures via applying current to it. A small bias regulates the emission of electrons from cathode, and positively charged anode attracts electrons and accelerates them toward the condenser lenses. There are two condenser lenses in microscope. The first condenser lens is responsible for demagnification of the focused electron beam produced in the area of electron gun. Final condenser lens does final demagnification of the spot, and is used mainly to calibrate the size of the beam without losing it. Microscope contains a stigmator that corrects any asymmetrical distortions of the electromagnetic

field, and two sets of deflection coils connected to the scan generator needed to scan the electron beam across the specimen. Once the beam hits the specimen and inelastically scattered electrons with the energies of 20-50 eV are ejected from the specimen at different angles, negatively charged secondary electrons are attracted to a positively charged secondary electron detector. Detector is surrounded by a Faraday cage maintained at 100-300 V, and has the end coated with aluminum and biased to 12 kV. The negatively charged electrons strike the aluminum coating with such impact that they pass through the layer, hit a scintillator material and generate a scintilla that then strikes a photocathode of a photomultiplier. Photoelectrons produced in photocathode pass through the photomultiplier, and generate the signal [29].

Elastically scattered electrons ejected from the specimen with energies similar to the energy of electron beam, travel in straight lines at high velocities. These electrons are called backscattered electrons and are detected by backscattered electron detectors installed underneath a final lens, around the open apertures. Backscattered electrons cause injection of electrons in the silicon diode, and produce the flow of current. Since this type of detector does not have a photomultiplier, electronic circuits are used to amplify the signal to the display. Such detectors are based on discrimination of the signal by atomic number contrast.

Electron gun

Anode

Alignment coils

Zoom condenser lens

Scan coils

Objective lens

Backscattered Electron Detector

Secondary electron detector

Specimen stage

High tension cable

① Electron gun chamber

Evacuation manifold

③ Objective aperture selector

Column isolation valve

Specimen chamber

Specimen exchange chamber

Backscattered electron detector

Specimen holder

Fig. 3. Schematics of scanning electron microscope [29].

The main difference between focused ion beam microscope and SEM is that the first uses a beam of ions instead of electrons. The source type used in the microscope was gallium liquid metal ion source (LMIS). The ion gun of the microscope consists of a tungsten needle placed in a contact with gallium, which when heated emits gallium

atoms as a result of ionization. In dual beam FIB/SEM systems, the electron and ion guns are placed at 52° incidence, while the chamber is shared between two.

CHAPTER III

SYNTHESIS OF CARBON NANOTUBES

3.1. Methods of Production of CNs

Arc-discharge method was used in the experiment that first produced carbon nanotubes [1]. Since that time, various different methods such as chemical vapor deposition (CVD), laser-ablation, catalytic CVD, plasma torch method, underwater alternating current (AC) electric arc method, and many other techniques were explored [1, 30-31]. A large scale production of defect free nanotubes is demanded for industrial applications, and in this chapter the principal methods of nanotubes production will be delineated.

3.1.1. Chemical Vapor Deposition Method

In CVD method, catalyst materials are heated to high temperatures (500 to 1200 ^{o}C) in a tube furnace, in which hydrocarbon gases are flowing for the specified periods of time. The MWNTs growth in CVD at the temperatures of 500 to 800 ^{o}C involves catalytic decomposition of hydrocarbon gases, such as acetylene (C_2H_2), ethylene (C_2H_4), xylene (C_8H_{10}) or benzene (C_6H_6), on catalytic nanoparticles such as nickel, cobalt and iron. Carbon required for nanotube growth is produced as a result of dissociation of the precursor hydrocarbon into the catalyst particles on the surface. MWNTs produced using CVD method, in case if they are of high density, can be aligned with others by the Van der Waals attraction forces, allowing growth of CNs perpendicular to the substrate. The typical schematics of CVD process is given in Fig. 4.

The main disadvantage of the CVD method is the high density of structural defects of carbon nanotubes that is believed to be because of the low temperatures used in the process.

Plasma enhanced CVD (PECVD) process is more commonly used in production of vertically aligned carbon nanotubes. In this process operating temperatures are substantially lower comparing to other methods since dissociation of precursors required for deposition is enabled by the high energy electrons. CN growth can be achieved using different sources of plasma. Experimental studies conducted in the past decade, report the following plasma sources: direct current (dc) [32-40], hot-filament aided with direct current [41-44], radiofrequency (rf) [45], microwave [46-56], inductively coupled plasma reactors [57-58] and rf with magnetic enhancement [59-60, 13].

Typical PECVD reactor set-up includes plasma source, power coupling components, mass flow controllers, vacuum pumps and a matching network. The substrate in the plasma reactor is heated directly by a heat source located underneath substrate holder, and walls of the reactor are maintained cold. Once wafer with the catalyst is loaded into the chamber, and a good vacuum is established, substrate holder is heated to the required temperature, and the feedstock is admitted. After, flow rate and chamber pressure can be aligned to the desired values, and power from the source is interlocked with the plasma. At the end of operation reactor is blasted with argon to decrease the temperature, because exposure to air at temperatures higher than 300 $^{\circ}$C leads to damaging carbon nanotubes [13].

Inert Gas

SAMPLE

FURNACE
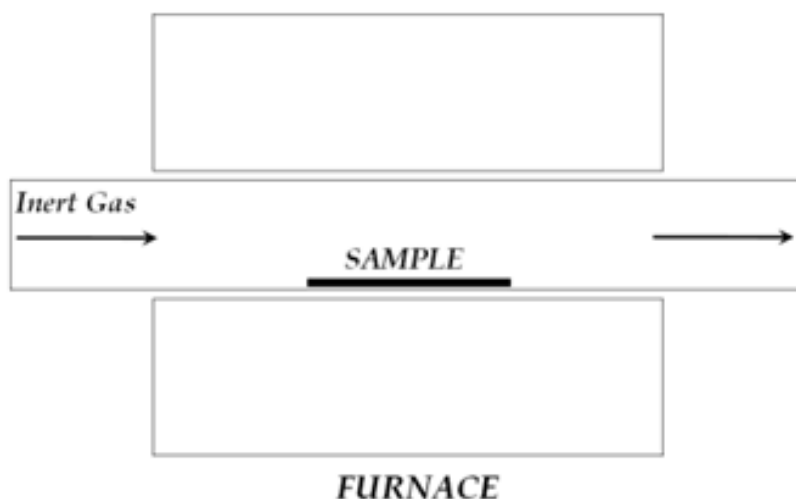
Fig. 4. Schematic representation of CVD method.

3.1.2. Arc Discharge Method

Arc discharge method is one of the oldest methods of production of CNs, which was used in discovering of carbon nanotubes by Iijima in 1991. The following description will be based on experimental setup used in first successful experiment on production of carbon nanotubes.

In arc discharge method two vertical electrodes (anode at the upper side and a cathode at the bottom) are located in the center of the chamber. Anode is produced from a graphitic carbon with the diameter less than that of a cathode. This cathode is made from a carbon with a shallow dimple that holds a piece of iron while evaporation takes place. A gas mixture consisting of methane and argon is used to fill evaporation chamber. Once the direct current runs between electrodes, discharge arc should be induced and iron filings should melt forming a droplet. Iron vapor generated from a

droplet condensed into small particles of iron carbide. It is well known that iron serves as a catalyst in many processes, including production of carbon nanotubes and carbon fibers since it acts as a heterogeneous deposition center for carbon atoms. The production of iron carbide is accompanied with the production of a smut from methane and by evaporation from the cathode [1]. A high temperature achievable in the process allows sublimation of carbon. After all procedures, wafer with carbon nanotubes on it should be purified by gasification with oxygen or carbon dioxide. The main disadvantage of this method is that the process is interrupted during removal of products from the chamber [13].

The first successful attempt to produce a large amount of CNs by the use of arc discharge method was done by Bethune et al. The process parameters used in their experiment were different from the process parameters used by Iijima [1, 50]. These parameters included high current values (100 A), voltage range (30-35 V) under specified electrode dimensions with the small gap between electrodes (>1 mm), and high temperatures of plasma (4000 K). See Fig. 5 in description of schematics of the reactor used in arc discharge method [50].
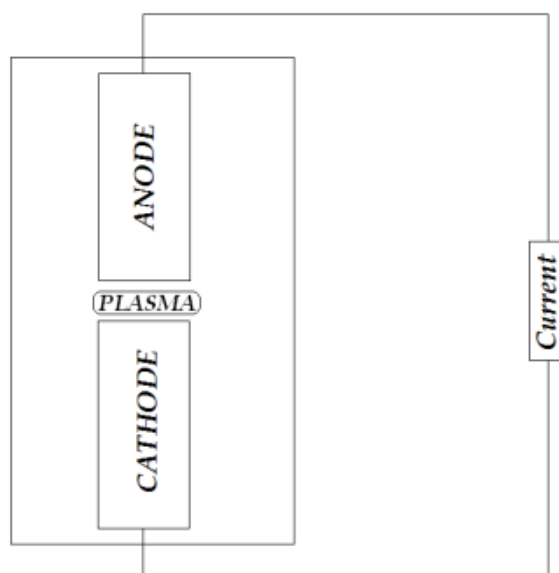
Fig. 5. Schematic representation of arc-discharge method.

3.1.3. Laser Ablation Method

In laser ablation method discovered by Guo and coworkers, a mixture of carbon and transition metals are evaporated by a laser impinging on a target, allowing better control conditions, and producing nanotubes of better quality and higher yield [51]. To sustain a uniform vaporization face, laser beam scanning across the target surface should be focused onto a metal-graphite composite target supported by graphite poles. Once vacuum is established in a tube shaped reactor, it is filled with argon to sweep the soot produced by laser vaporization from high temperature zone to the water cooled copper collector. For schematic representation of the process see Fig. 6. High temperatures are obtained by the use of the furnace mounted to the flow tube [61].

Arc discharge and laser ablations methods are similar in a sense that they have same advantages such as high yield of SWNTs, and disadvantages such as their dependence on evaporation of carbon atoms at temperatures exceeding 3000 ^{o}C and interlaced nature of nanotubes that are difficult to purify. Carbon nanotubes prepared using laser ablation method, dominantly are single-walled, highly tangled, and nearly endless [33]. A large amount of nanoscale impurities such as fullerenes, onions, and amorphous carbon, and polyhedral graphite nanoparticles are produced along with production of CNs in this method. Since these impurities are difficult to separate from nanotubes after they are cut, purification plays a very important role in laser ablation method as well as in arc discharge method.
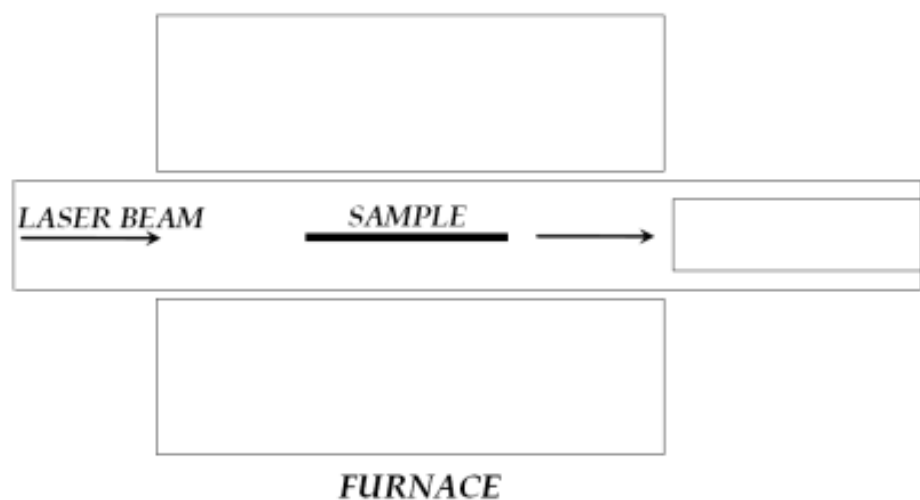
Fig. 6. Schematics of laser ablation method.

Production of CNs in a controlled way and in large amount encounters problems, which remains to be solved. At this time, low-temperature CVD method is becoming a strong candidate for the large scale production of carbon nanotubes. One of the main advantages of this method is the ability to arrange carbon nanotubes into well-defined configurations by controlling catalyst positioning. The level of control provided by this method enables the construction of complex carbon nanotubes architectures, which could lead to the nanotubes based devices and systems in a scalable fashion [13].

3.2. Preparation of Carbon Buckypapers

Prior to preparation of carbon buckypapers, carbon nanotubes should be purified to attain better susceptibility of nanotubes to aqueous procedures. Purification of CNs is required to dissipate residual catalyst particles, and mostly is done in hydrochloric acid (HCl), sometimes with the addition of nitric acid to the etch which improves purification process. Acid treatment and consequent ablution with de-ionized water (to neutralize nanotubes) leads to the next step − filtration. Once the nanotubes are filtered, they are dried and milled (reground) into a powder [62].

Carbon nanotube powder obtained after purification has to be suspended in deionized water by exploiting surfactants such as sodium dedocyl sulfate (SDS) and Triton X, and sonicated to ensure deficiency of agglomerations, and proper dispersion of nanotubes in the suspension. This method provides a suspension enduring the same condition for several months without precipitation. It is worthy to note that efficiency of

an ultrasonic tip is higher than the efficiency of an ultrasonic bath for the following

reason: time demanded to disperse nanotubes using ultrasonic tip is less than the time

obligated to do it in ultrasonic bath. Since longer processing time causes shortening of

nanotubes, ultrasonic tip is used in most cases [62].

Obtained suspension is injected into the dead-end filtration unit. There are

several methods of filtration of carbon nanotubes. The vacuum filtration process in

which suction on the filtrate side controls filtration and gravity is used to assist in

settling of suspension prior to applying vacuum. The other method implies using

filtration unit in which high liquid pressure produced from pumping is applied to achieve

passage of suspension through the filter [63]. Once the suspension is traverses through

the filter, nanotubes will be deposited in the surface of the filter that evolves into a

continuous sheet composed of CNs. The thickness of buckypaper is determined by the

concentration and volume of the suspension outgoing filtration. Filtration and

subsequent deposition of CNs is followed by removal of obtained carbon buckypaper

from the supporting filter membrane [62].

In the experiments presented in this work, free-standing carbon buckypapers

were of ~100 micrometers in thickness since buckypapers with lower thickness (<50

um) are laborious to manage and remove from the filter membrane. The schematic

representation of the carbon buckypapers' preparation process is shown in Fig. 7. The

preparation of buckypapers with lower thickness usually does not involve removal of

buckypaper from supporting filter. The filter membrane types suitable for preparation of

carbon buckypapers on a supporting film are polycarbonate filter membranes, Nylon,

and aluminum oxide membranes [63]. Production of thin free standing papers can take place when using very long carbon nanotubes (>50 um) in the process.
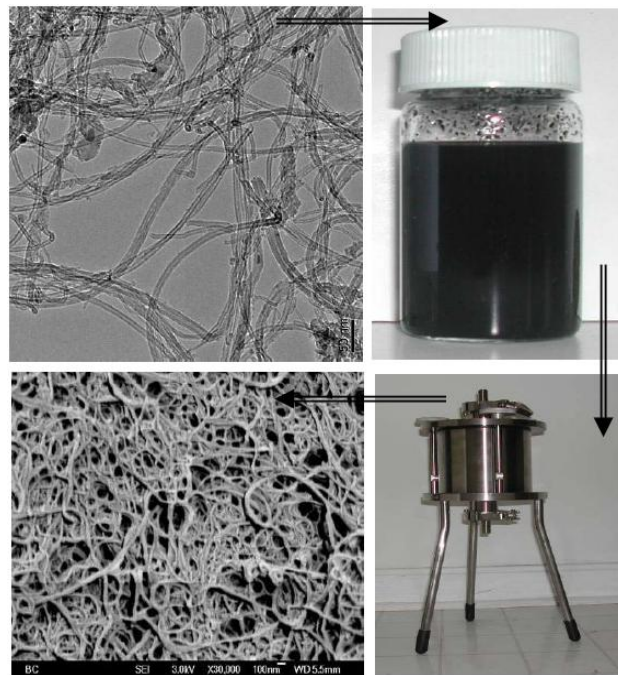
Fig. 7. Schematics of preparation of carbon buckypapers [62].

CHAPTER IV

# MECHANISM OF DAMAGE FORMATION UNDER IRRADIATION

The knowledge and comprehension of the energy loss mechanisms is crucial in estimating depth profile of incident ions, evaluating lattice disorder created upon irradiation, and obtaining a better control of implantation conditions. Energetic particles withstand a chain of collisions with atoms and electrons of the material they are passing through. Interactions of penetrating particles with electrons and atoms of target material involve energy loss (*dE/dx*) governed by Coulomb's law.

There are two known energy loss mechanisms: nuclear collisions, and electronic collisions. Schematic representation of the energy loss mechanisms in a target material can be seen from Fig. 8. Amount of energy reduction per unit length, i.e. energy loss rate can be written as a sum of the energy loss rate by nuclear and electronic collisions:

$$\frac{dE}{dx} = \frac{dE}{dx}\big|_n + \frac{dE}{dx}\big|_e \qquad (4.1)$$

where subscripts *n* and *e* symbolize nuclear and electronic collisions, respectively.

Nuclear energy loss rate known as amount of energy moving particles lose in elastic collisions per unit length is of great importance in low energy region. In nuclear collisions energy is transferred to a target atom completely, with large losses of energy, and essential angular deflections. These collisions can lead to the displacements of atoms from their lattice sites, and consequent formation of lattice disorder.
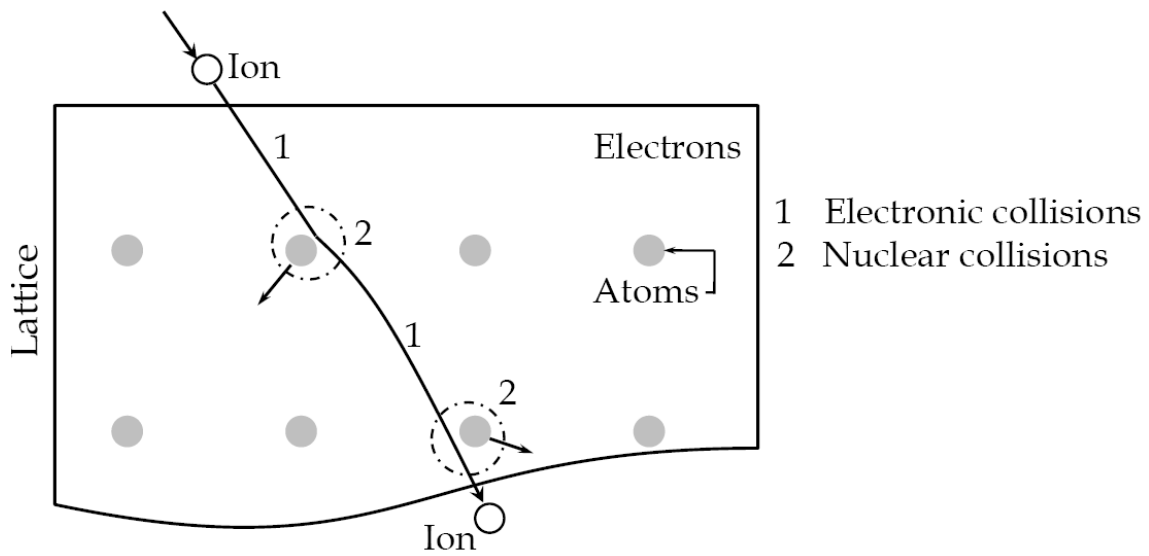
Fig. 8. Energy loss mechanism of incident ion.

Electronic collisions in which impinging particles excite or eject electrons of the target material, are responsible for insignificant lattice disorder, and minor angular deflections of trajectories, since smaller energy losses per collision are involved. It should be noted that while nuclear collisions prevail for low energies and high atomic numbers of elements, electronic collisions dominate for high energies and low atomic numbers. A comparison between nuclear and electronic energy losses can be observed in Fig. 9.

Nuclear energy loss dominates when ion velocities υ are lower than velocity of atomic electrons υ_0 (Bohr velocity) since at these velocity values ion carrying its electrons neutralizes by capturing electrons. Nuclear energy loss decreases as $1/E_0$ with increasing velocity of ions, and electronic energy loss starts to prevail at a certain point.

Electronic energy loss is proportional to $E^{1/2}$ in the velocity range from $0.1v_0$ to $Z_1^{2/3}v_0$, and at $v \geq v_0 Z_1^{2/3}$ ion will be stripped of all electrons since the charge state of ion increases with velocity. Once velocity passes given threshold, ion can be thought as a positive point charge Z_1 that possesses velocities exceeding the mean orbital velocities of electrons in target atom [64].
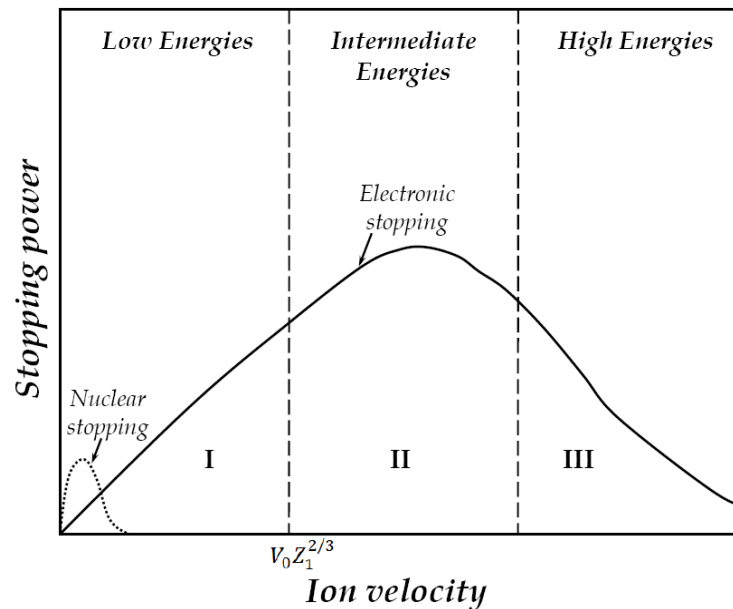
Fig. 9. Nuclear energy loss vs. electron energy loss.

As impinging ion slows down in a solid, it undergoes collisions with atoms in a lattice. At this point, radiation damage event should be considered in more details. Radiation damage event is believed to be a transfer of energy from penetrating particles to target material with consequent allocation of atoms. It includes the following:

interactions between energetic particle and lattice atoms, displacement of lattice atoms by incident particles via transfer of kinetic energy, displacement of atoms from their lattice sites by primary knock-on atoms (PKAs) and creation of additional PKAs, all of which results in formation of displacement sequence of collision events known as displacement cascade. Once PKA becomes an interstitial in a lattice site, damage event is treated to be complete, and propagation of vacancies, interstitial atoms, and defect clusters in the region of the ion track are considered to be the result of such event. This phenomenon impacts mechanical and physical properties of the material. As it can be seen from Fig. 10, these events take place in time interval of 10^{-11} sec.
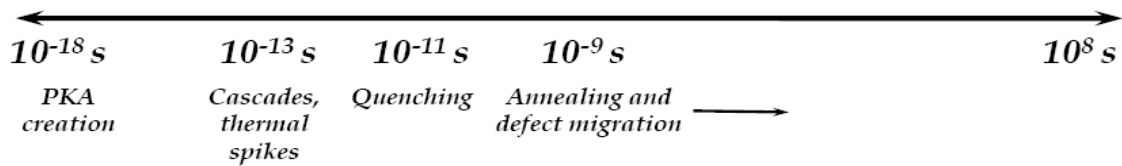
Fig. 10. Time dependence of the chain of radiation damage events created in material.

Displacement of target atom from its lattice site and subsequent formation of a stable interstitial takes place only if atom receives a certain minimum amount of energy from an energetic ion in a collision. Energy demanded for a displacement to take place is known as displacement energy E_d and it corresponds to the threshold of displacement. Displacement energy confides on the direction of target atom's momentum. Depending on the amount of energy transferred to a lattice atom (T), ensuing processes can occur:

a) if $T<E_d$, target atom will remain at its lattice position but will be subjected to the large-amplitude vibrations, releasing energy as phonons and appearing as a localized source of heat; b) if $T>E_d$, displacement of a target atom with subsequent formation of a vacancy will betide, and an interstitial site in the lattice will be occupied by a displaced atom. The mentioned vacancy-interstitial defect is pertained to a Frenkel pair.

In analysis of spatial distribution of point defects produced during slowing down of an atom or a PKA, average distance traveled by energetic particle between displacement collisions with target atoms, so called mean free path λ_d, is one of the most important parameters. Mean free path of an ion slowing down in a target decreases to the point when PKA is produced at every lattice site onward path of an ion. Once mean free path of an ion and PKA reaches interatomic spacing, a large number of defects will be generated in a very short period of time, and damage cascade cannot be treated as agglomeration of isolated point defects such as vacancies and interstitials. At this stage, high density cascade in a limited volume with the most part of atoms in impermanent motion, defined as spike should be taken into account (see Fig. 11). According to the investigation of Brinkman, highly damaged region will be formed when λ_d is comparable to atomic spacing of the target atoms. In this damaged region displaced atoms are extruded form the path of incoming ion or PKA, which result in formation of a volume consisting of a shell of interstitial atoms enclosing a core of vacancies. Important parameters also include the time required to form a displacement spike which is analogous to the time needed for an ion or PKA to come to rest, and the critical energy E_c. If the energy of PKAs or ions is lower than E_c, a single dense cascade or

displacement spike formation is favored, and if their energy exceeds E_c, formation of a subcascade will be preferred.

It can be seen from the previous discussion, that by the end of the displacement spike, energy of displaced atoms decreases so that no further displacements can be tracked. Energy of collisions will be distributed among neighboring atoms in high deposited energy density region, and released as lattice vibrations. This interval is called a thermal spike stage. In the next stage named quenching, energy is transmitted to surrounding atoms and stable lattice defects are produced. After quenching phase, mobile defects are able to leave cascade region, and create more comprehensive defects. For the time scale of the cascade stages see Fig. 10.
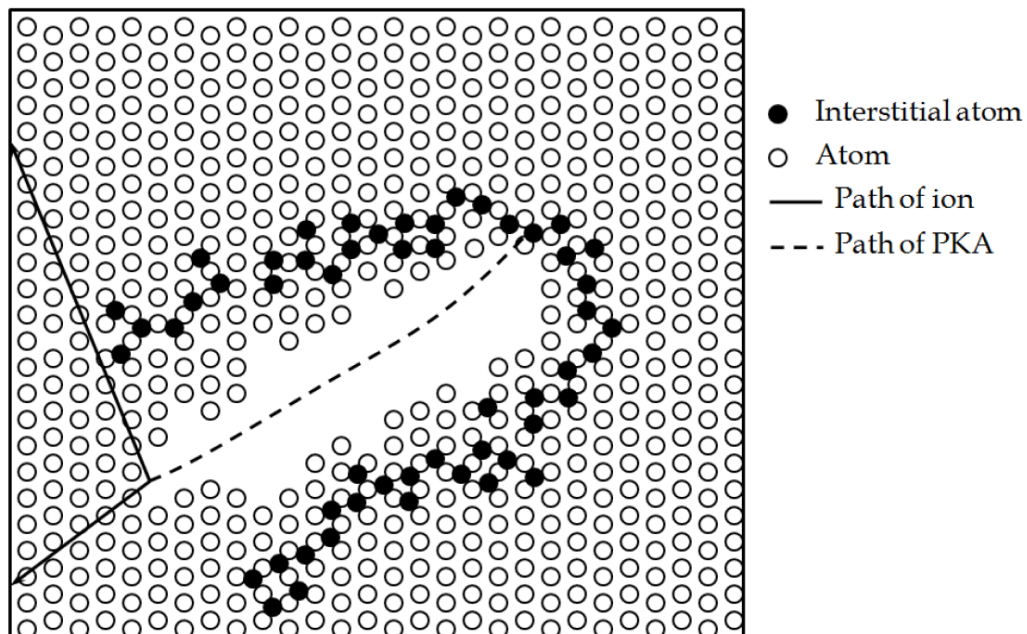
Fig. 11. Displacement spike.

A proper understanding of forces between two colliding atoms is critical for determining radiation damage event. Interaction between atoms is described via potential functions. Since nuclear charge is screened by electrons, in case of atoms where nucleus is surrounded by electron clouds of opposite charge, Coulomb potential defining potential energy between two point charges placed at some distance r from each other, should be modified by a screening function $\chi(r)$.

$$V(r) = \frac{z_1 z_2 e^2}{r} \chi(r) \tag{4.2}$$

As it can be seen from Fig. 12, interatomic potential changes with separation distance. Interaction is driven by Coulomb forces at large separation distances, while at smaller separations repulsive central field force prevails. In order to calculate interatomic potential, one must first consider Coulomb's interaction between nuclei and electron, then shell structure of electrons, and Pauli's exclusion principle stating that no electron can occupy the same quantum states and exchange interaction of electrons.

Kinchin-Pease model is used to calculate the number of atoms translated by PKA possessing some energy (T) in a solid lattice. The model relies on the following assumptions:

    a. A sequence of two-body elastic collisions between atoms results in formation of a cascade.

    b. For energies (T) exceeding minimum amount of energy that should be transferred to cause a displacement (displacement energy E_d), probability of a displacement is equal to 1.

c. Cut-off energy (E_c) represents the energy loss through electron stopping. Supplementary displacements do not take place if energy of PKA surpasses cut-off energy. Electronic stopping is neglected for all energies less than E_c while atomic collisions are considered.

d. Crystal structure and associated effects are ignored; positions of atoms in a solid are regarded to be random.
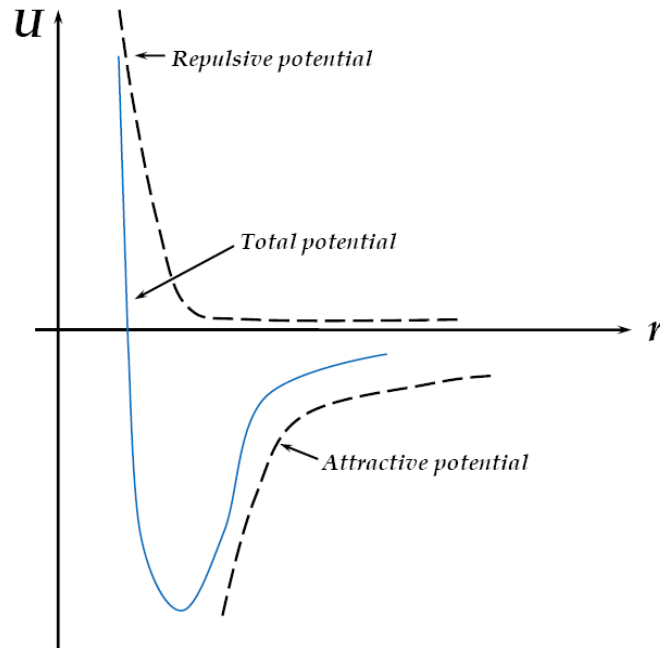
Fig. 12. Variation of interatomic potential with separation distance.

The Kinchin-Pease model is formulated in the following way (Eq. 4.3), and schematic representation of the dependence of the number of displaced atoms to the PKA energy based on Kinchin-Pease model is given in Fig. 13.

$$\text{Number of displacements} \quad \begin{cases} 0 & \text{for } T < E_d \\ 1 & \text{for } E_d < T < 2E_d \\ \dfrac{T}{2E_d} & \text{for } 2E_d < T < E_c \\ \dfrac{E_c}{2E_d} & \text{for } T \geq E_c \end{cases} \quad (4.3)$$
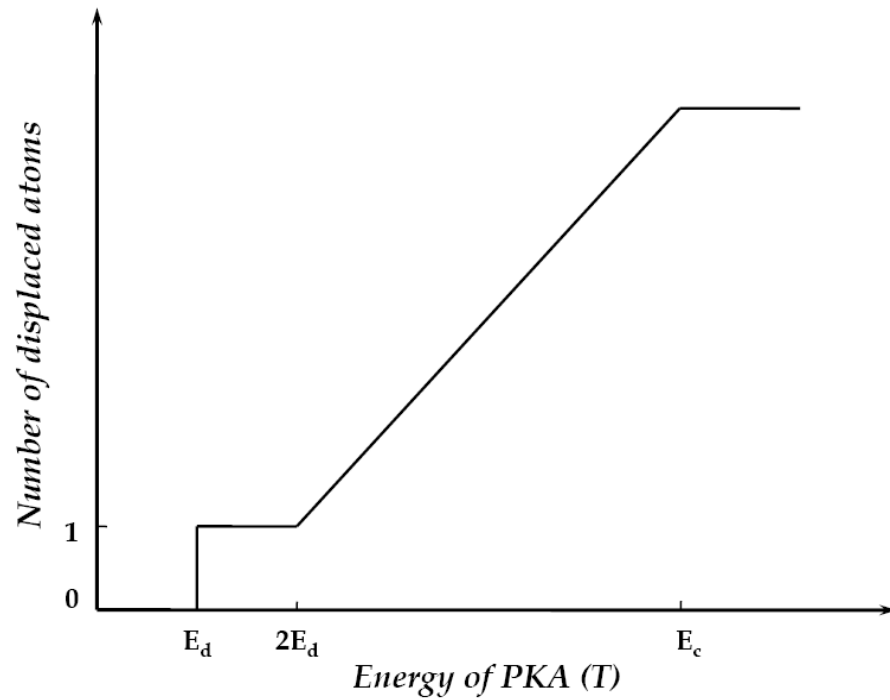
Fig. 13. The number of displaced atoms vs. PKA energy based on Kinchin-Pease model.

A displacement per atom (dpa) is a measure of irradiation damage noting that each atom in a volume subjected to irradiation has been translated from its equilibrium position at least once. Displacement per atom at depth x (*dpa(x)*) per unit dose can be

estimated by using Kinchin-Pease model based on assumption that number of displacements per unit depth at a depth x ($N_d(x)$) can be expressed through this model:

$$dpa(x) = \frac{0.4F_D(x)}{NE_d}\varphi \tag{4.4}$$

where $F_D(x)$ is the deposited energy depth distribution function, N is the number of displacements, φ is an ion dose (ions/cm^2), and E_d is the displacement energy [64].

Now, consider interaction of defects in multi-walled carbon nanotubes. Priority of defect interactions predicted in MWNTs after irradiation can be seen in figure given below (Fig. 14). After production of point defects in irradiated MWNTs two processes can take place: recombination of defects giving rise to dynamic recovery or defect migration resulting in generation of defect clusters. Migration of defects toward internal sinks and surface can be anticipated at longer irradiation times. Resistivity values are affected by these reactions at different time scales.

In order to understand mechanism of interactions between point defects and various defect aggregates, one should refer to the reaction rate theory [65-66]. Fenkel defects, produced in a sequence of collisions between impinging particles and lattice atoms, can be lost in two different processes: through reaction with a defect sinks such as voids and dislocation, and via recombination of interstitials and vacancies.
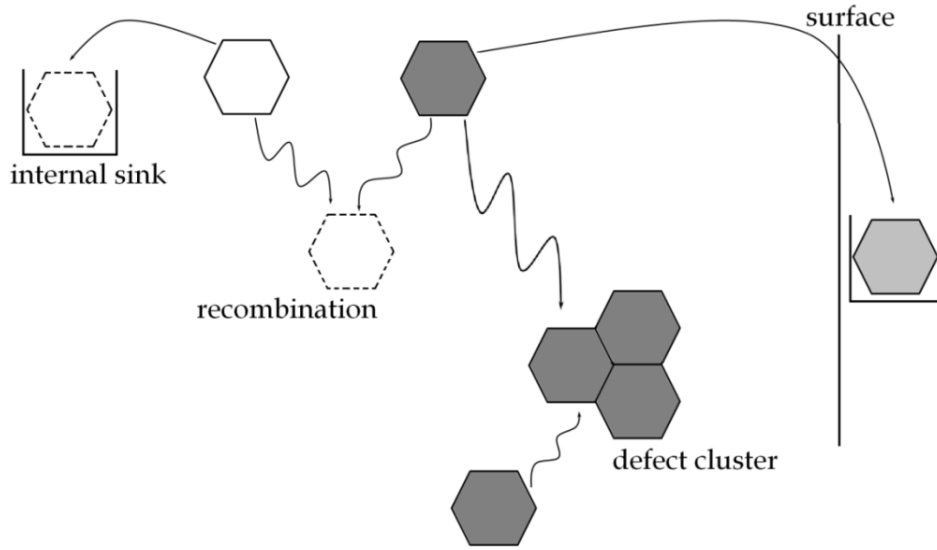
Fig. 14. Schematic representation of interactions of defects in MWNTs after irradiation.

Concentration of point defects at any point and time implies the balance between their production and loss rates. Variation of defects concentrations can be thought of as sum of the following parameters: a) local production rate, b) reactions with other species such as interstitial-vacancy recombination and reactions with sinks, and c) diffusion from or into the local volume. This can be represented by the following simplified equations:

$$\frac{\partial C_v}{\partial t} = K_0 - K_{iv}C_iC_v - K_{vs}C_vC_s + \nabla D_v \nabla C_v$$

$$\frac{\partial C_i}{\partial t} = K_0 - K_{iv}C_iC_v - K_{is}C_iC_s + \nabla D_i \nabla C_i \qquad (4.5)$$

where C_i and C_v are the concentrations of interstitials (*I*) and vacancies (*V*), t is time, K_0 is the defect generation rate that is responsible for creation of freely migrating defects

leading to the long-range diffusion, K_{iv} is the interstitial − vacancy recombination rate coefficient, K_{vs} and K_{is} are the vacancy − sink and interstitial − sink recombination rate coefficients, C_s is the sink concentration, D_i and D_v are interstitial and vacancy diffusion coefficients, respectively.

Considering $D_i \gg D_v$, the rate constants can be written as follows:

$$K_{iv} = 4\pi r_{iv} D_i$$

$$K_{is} = 4\pi r_{is} D_i \qquad (4.6)$$

$$K_{vs} = 4\pi r_{vs} D_v$$

where r_{iv}, r_{vs}, and r_{is} are interaction radii for the interstitial-vacancy, vacancy-sink, and interstitial-sink reactions, respectively. These represent the radii of the surfaces that will be annihilated when crossed by defects.

Initially, defect concentrations are not sufficient to affect buildup, so they increase as $dC/dt = K_0$ with $C_i \sim C_v$, such that $C_i = C_v = K_0 t$. Once recombination rate starts to compensate production rate, the buildup of point defects will stop its linear increase. For interstitial defects, its time dependent changes are given by:

$$\frac{\partial C}{\partial t} = K_0 - K_{iv} C^2 = 0 \qquad (C = C_i = C_v) \qquad (4.7)$$

This equations leads to the following solution:

$$C = \left(\frac{K_0}{K_{iv}}\right)^{\frac{1}{2}} \qquad (4.8)$$

By taking this concentration and solving Eq. (4.7), time at which production and recombination rates start compensating each other, can be obtained:

$$t = \tau_1 = (K_0 K_{iv})^{-\frac{1}{2}} \qquad (4.9)$$

where τ_1 is the characteristic time for the onset of mutual recombination.

After a certain period of time, interstitials and vacancies will start finding sinks, which augment annihilation. It is evident that interstitials are lost to sinks in greater amounts than vacancies by recalling $D_i \gg D_v$, which can be seen from the next equation:

$$\frac{dC_i}{dt} = -K_{is}C_iC_s \tag{4.10}$$

Since concentration of interstitials decreases more rapidly and vacancy concentrations increase because of the rapid decay of only sink of vacancies, solutions will have the following form:

$$C_v = \left(\frac{K_0}{K_{iv}}\right)^{\frac{1}{2}} = \left[\frac{K_0 K_{is} C_s t}{K_{iv}}\right]^{\frac{1}{2}}$$

$$C_i = \left(\frac{K_0}{K_{iv}}\right)^{\frac{1}{2}} = \left[\frac{K_0}{K_{iv}K_{is}C_s t}\right]^{\frac{1}{2}} \tag{4.11}$$

From these equations, time constant for onset of the buildup regime can be determined:

$$t = \tau_2 = (K_{is}C_s)^{-1} \tag{4.12}$$

A true steady state (ss) will be achieved when the vacancies start interacting with sinks, which can be written as:

$$C_v^{ss} = -\frac{K_{is}C_s}{2K_{iv}} + \left[\frac{K_0 K_{is}}{K_{iv}K_{vs}} + \frac{K_{is}^2 C_s^2}{4K_{iv}^2}\right]^{\frac{1}{2}}$$

$$C_i^{ss} = -\frac{K_{vs}C_s}{2K_{iv}} + \left[\frac{K_0 K_{vs}}{K_{iv}K_{is}} + \frac{K_{vs}^2 C_s^2}{4K_{iv}^2}\right]^{\frac{1}{2}} \tag{4.13}$$
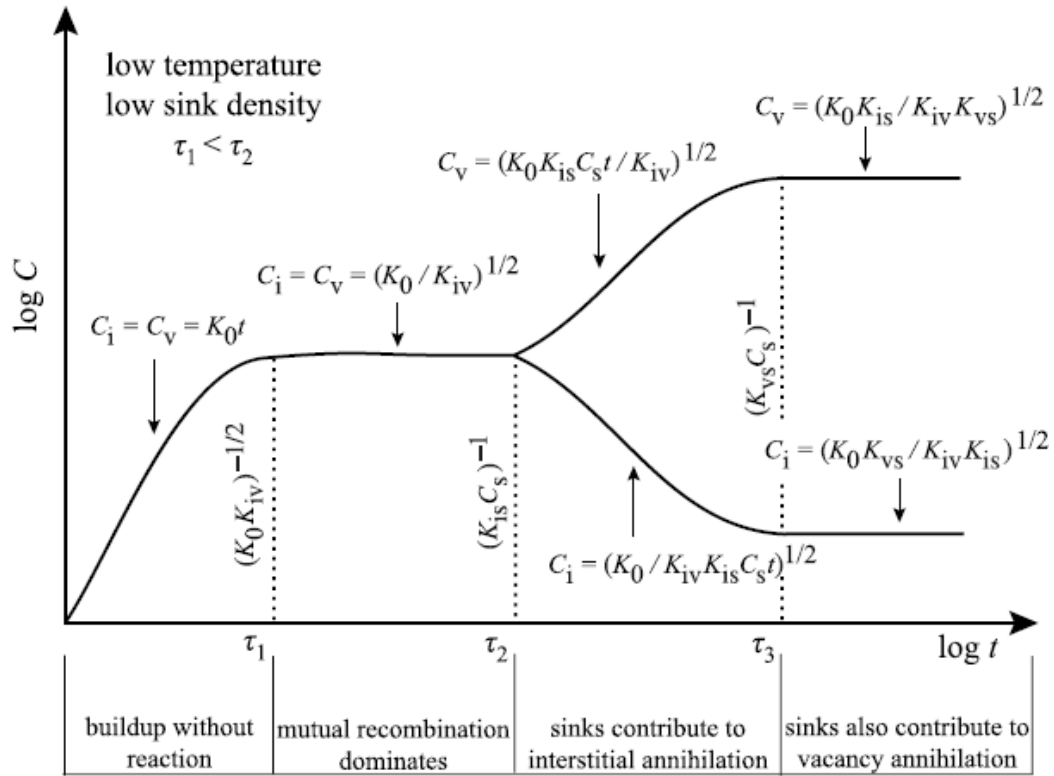
Fig. 15. Concentration of vacancies and interstitials as a function of time [66].

Considering that at steady state, when production and loss rates of interstitials and vacancies are equal, loss of vacancies and interstitials should be equal as well. At low temperature and low sink density, terms including C_s can be neglected, and concentrations of vacancies and interstitials become:

$$C_v^{ss} \cong \sqrt{\frac{K_0 K_{is}}{K_{iv} K_{vs}}} \qquad \text{and} \qquad C_i^{ss} \cong \sqrt{\frac{K_0 K_{vs}}{K_{iv} K_{is}}} \qquad (4.14)$$

By taking these expressions to the equations written for buildup region, concentration of vacancies alter to:

$$C_v = \left[\frac{K_0 K_{is} C_s t}{K_{iv}}\right]^{\frac{1}{2}} = \left[\frac{K_0 K_{is}}{K_{iv} K_{vs}}\right]^{\frac{1}{2}} \tag{4.15}$$

Subsequently, time constant for onset of steady state transforms to:

$$t = \tau_3 = (K_{vs} C_s)^{-1} \tag{4.16}$$

The schematic representation of the buildup is given in Fig 15. However, it should be noted that transitions between phases are not as sudden, as it is shown in a figure. Note that if the sink density is neglected by assuming that it s equal to zero, the exact solution of the initial equation (Eq. (4.5)) will give [66]:

$$C_v(t) \approx \sqrt{\frac{K_0}{K_{iv}}} \tanh\left(\sqrt{K_0 K_{iv}} t\right) \tag{4.17}$$

As it was discussed previously, irradiation of any type of solids with energetic particles leads to formation of defects and subsequent disintegration of irradiated matter. Irradiation response of carbon nanotubes is different from that of bulk solids, not only because of their small size but also because of their ability to reconstruct under irradiation. In bulk solids irradiation with energetic particles results in inelastic interaction of incoming particles with atoms of a target material and absorption of energy, while in nanostructured materials energetic particles penetrate through without having inelastic interactions with target atoms. As a result, only a small amount of energy is deposited, energy loss of incident particles is small, and higher energy of bombarding particles introduces smaller energy loss. By not taking into consideration displacement cascades, it can be assumed that amount of damage should be less in nanostructured materials if energy of impinging particles is high [17]. However, small size of objects leads to the issues such as high temperature profile created by particle

bombardment (temperature can surpass melting temperature of the target), changed electronic structure and mechanism of transformation of electronic excitation to kinetic energy, and high sputtering yield [5].

Irradiation can cause formation of irradiation-induced links between nanotubes which might result in increased conductivity of material or decreased conductivity in the defective regions of the nanotubes [67-69]. Materials can deteriorate in different ways depending on the types of defects.

Sputtering is substantial for SWNTs. If the value of energy transfer exceeds the threshold value, carbon atom evaporation from the surface takes place, and vacancies will be major type of defects occurring in the system. Unlike in other types of materials, open structure of nanotubes can cause displacement of recoils to the long distances if energy slightly above the threshold is applied. When concentration of vacancies surpasses a certain value, structural transformation to an amorphous phase is expected.

CHAPTER V

MOLECULAR DYNAMICS SIMULATIONS OF

IRRADIATION EFFECT ON CNs

Defects in CNs can be generated if energy of incident particle is higher than threshold energy, which is the minimum energy bombarding particle transfers to atom to create a Frenkel pair that will not recombine spontaneously. In SWNTs vacancies and primary knock on atoms are formed as a result of collisions between incoming energetic particles and carbon atoms. If energy of those knock on atoms is high enough, they tend to leave tube or displace neighboring atoms, and if energy is low they can be adsorbed onto the walls of tubes and serve as interstitials. However, since quasi one dimensional morphology of nanotube network dictates that no interstitial can exist in the system, sputtering of all displaced atoms from nanotubes can befall. Further damage of network is created by sputtered carbon atoms and impinging particles. Immediate interstitial vacancy recombination is averted by large separation distance occurring because of the presence of voids in a sample. It is also assumed that interstitial atom in bundle of SWNTs can be thought as an adatom adsorbed on the surface of nanotube. In conjunction with these defects, complex defects such as Stone-Wales (SW) defects [17, 70], topological defects in graphitic network and amorphous complexes can be produced after bombardment with energetic particles [71]. The most dramatic defects produced in nanotubes under impact of irradiation are considered to be the following: adatoms playing role of interstitials, and vacancies [17, 72].

It is well known that damage production is higher in case of ion irradiation because of the higher probability of vacancy clusters formation. Under energetic ion bombardment carbon nanotubes degrade and simultaneously heal the defects via dangling bond saturation and adatom migration [73]. So nanotubes have a unique feature to anneal defects created under energetic particle bombardment. There are two possible explanations of defect annealing in CNs: 1) interstitial-vacancy recombination caused by migration of adatoms, and 2) mending of vacancies invoked from saturation of dangling bonds, formation of non-hexagonal rings, and production of Stone-Wales defects [73].

Knowledge of ion ranges in MWNTs is of great practical importance. Because of their more complex geometry, MWNTs received much less attention than SWNTs. Molecular dynamics study of capability of MWNTs to stop noble gas ions of different energies, conducted by Pomoell et al., has shown that impact of 1.25 keV Xe ion terminated production of interstitials between shells and vacancies on the walls of nanotubes. If under heavy ion bombardment (such as Xe) two vacancies appear in neighboring shells, atom extending out of boundaries can induce covalent bonds between shells which is similar to graphite. Impinging energetic ion transfers energy to atoms mostly in upper shells, and produces major carbon recoils and vacancies. Collisions of carbon recoils with carbon atoms in other shells leads to formation of higher number of recoils, and thus in higher damage of the system. All of the reasons given above can cause generation of an amorphous region [74].

Experimental results confirmed that irradiation with ions to high doses causes gradual amorphization of the nanotubes [75-77]. Theoretical studies testified dependence

between damage produced in CNs and irradiation doses [78]. Once number of defects reaches saturation, an amount of disorder builds up to the value at which impinging energetic ion does not cause any changes. It has been shown experimentally, irradiation of carbon onions with energetic ions and electrons result in formation of diamond nanocrystals [79]. As it was proved theoretically, tubular shape of MWNTs prevents the graphite-to-diamond transformation [74].

Simulations of interactions between SWNTs and different types of incident ions of low energies had demonstrated sputtering of carbon atoms from SWNTs, formation of single and multiple vacancies, and rapid increase of the amount of damage with incident ion energy. As it was proved, irradiation induced damage is higher for heavy ions and it can be explained in terms of the defect production cross section values in SWNTs. For instance, He ions create less defects since the cross section value is low, and Kr and Xe ions create more defects because of their approximately equal high value of cross section for the defect production [74].

MD studies of the ion irradiation of SWNTs on different substrates demonstrated that generation of defects at low temperatures depends on the type of substrate. Irradiation of CNs on metallic substrates consisting of heavy atoms produces more damage than in case of the nanotubes on light atom substrates because of the sputtering of substrate atoms and backscattering of carbon recoils. Increase of the amount of defects with increasing energy of incident ions to the certain value was observed. Once the energy of impinging ions reaches a certain level, number of defects does not change. This can be explained by dependence between nuclear collision cross section and ion

energy, at a certain value of ion energy cross section of nuclear collisions starts decreasing. According to predictions, nanotubes can be pinned to essentially any type of substrates under irradiation by establishing chemical bonds in the neighborhood of irradiation-induced defects [73, 78-79].

CNs are damaged by electron beam predominantly by single vacancies and interstitials. Molecular dynamics study aimed to reckon temperature dependence of concentration of point defects produced in TEM under electron bombardment showed strong dependence between these parameters. As it has been discovered, amount of vacancies increases quickly at low temperature ranges with temperature interval at which increased vacancy mobility leads to formation of immobile multi-vacancy structures and reduced self-healing under heat treatment. Vacancy mobility increases with temperature, and vacancies are able to escape from irradiation area and in-situ annealing of irradiation induced defects can occur. Mobility of single vacancies results in lower concentration of defects since vacancies can leave the area of irradiation prior formation of larger defects. Initially concentration of vacancies and adatoms are equal but different migration rates and sputtering increases difference between them. At high temperatures adatoms become more mobile and can leave the system, and at even higher temperatures all adatoms leave tubes [72]. However, all theoretical predictions should be proven experimentally to be reliable. For this reason, further focus of this thesis will be on experimental work.

CHAPTER VI

IRRADIATION OF CARBON NANOTUBES

In the last few years, ion irradiation of carbon nanotubes attracted attention of scientists for several reasons. One of these reasons is the need to develop a low cost and high efficiency method of controlling nanotubes' electronic, mechanical and magnetic properties. Advantages of using ion irradiation instead of conventional chemical methods are as follows: capability of focusing ion beams to the few nanometers in diameter spots, scanning over large areas, and possibility of combining ion irradiation with post irradiation annealing to repair created damage. Also ion doping can be used to tailor properties of materials. Ion irradiation can evaluate stability and functionality of CNs in harsh environments [64, 17]. As it has been shown, irradiation is able to a) form stable covalent links between carbon nanotubes causing enhancement of shear modulus of SWNTs [12, 14], b) cut CNs [15], c) transform SWNTs bundle into MWNT, and d) induce high pressure inside of tubes resulting in phase changes inside the core of nanotubes.

As it was pointed out in a previous chapter, electrons penetrating the solid interact with electrons and nuclei of the target material. Displacement of an atom by electron-nucleus scattering requires high electron energy because conservation of momentum allows a transfer of a small amount of energy from bombarding electrons to the nucleus. The value of energy needed to displace an atom (threshold energy) was already noted in the previous chapter, which for carbon atom is equal to 20 eV.

Ionization and bond breaking occurring at low energies of impinging electrons originate from electron-electron scattering. As a consequence of local reactions, target can be damaged.

Despite all the work conducted on studying irradiation effects in CNs and CNs based materials, radiation damage in CNs is still lacks fundamental understanding. Since CNs are considered to be potential material that can be used in nanostructured devices, irradiation response and stability of CNs are of great importance.

6.1. Irradiation of CNs in Microscopes

Irradiation-induced defects, as well as native defects in carbon nanotubes can be identified using several techniques experimentally. In situ generation and evolution of defects in real time is possible in transmission electron microscope (TEM), and detection of irradiation-induced morphology changes can be done in scanning electron microscope (SEM) [29]. Previous studies concentrating on electron irradiation of CNs, which were mostly carried in TEM, reported perforation of outer shells of the tubes, bending, and adjustment of diameters of CNs. The Ga ion beam was used to thin, slice and alter MWNTs at precise locations. Defects are induced in CNs during characterization in microscopes, which means that damage formation mechanism in CNs should be studied in details. In order to understand the damage formation mechanism in CNs, MWNTs were subjected to electron beam in SEM, and ion beam in focused ion beam (FIB) microscope operated at an accelerating voltage of 30 keV.

Figures 16-a and 16-b show secondary electron (SE) images of MWNTs bombarded with electrons at t=1min and t=15 min, respectively. The series of SE images were acquired in SEM after certain irradiation periods. The study shows that branched CNs experienced shrinkage after t=15 min. The arrows in Fig. 16 provide the guidance to notice shrinkage of MWNTs under electron irradiation. It is worth noting that, as observed in Fig. 16-b, a split in the branches of MWNTs occurred.
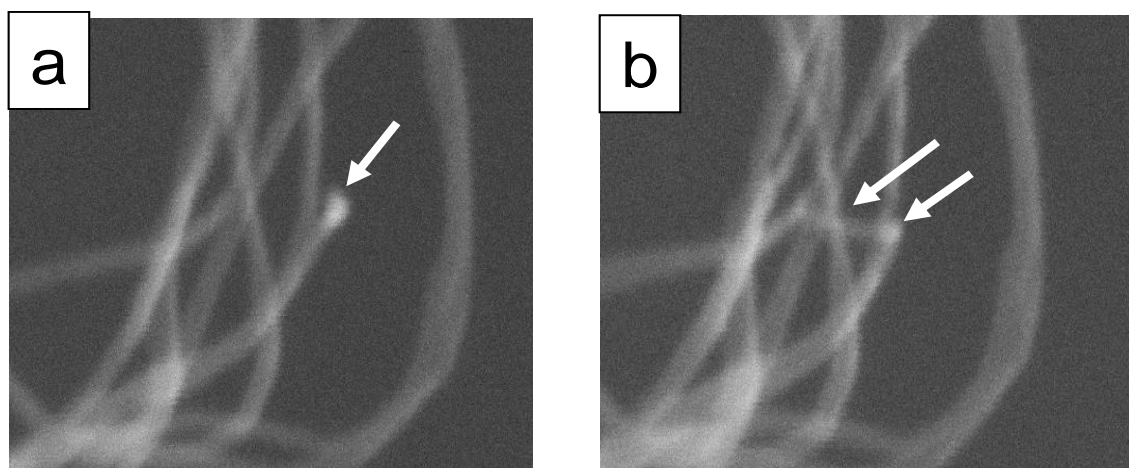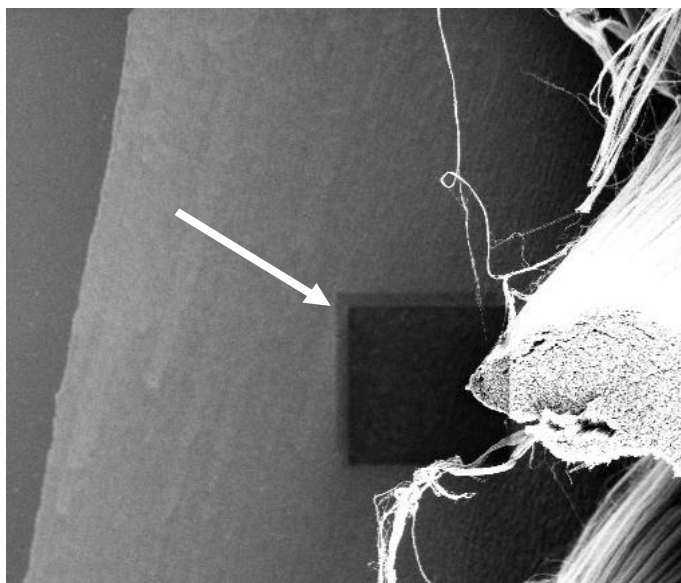

Fig. 16. SE images of MWNTs bombarded with electrons: a) image obtained after t=1 min, and b) after t=15 min of electron bombardment.

The phenomenon mentioned above can be explained by atom loss during irradiation and posterior shrinkage of individual shells, which is a result of surface reconstruction and dimensional changes caused by atomic rearrangements in the lattice of irradiated CNs. The underlying mechanism has been discussed in previous studies

[78, 80]. The shrinkage of carbon nanotubes under electron irradiation was previously observed, and theoretically studied, by using tight-binding molecular dynamics simulations (TBMD) by Ajayan et al. [80]. According to the simulations, shrinkage can be explained by recombination of "dangling bond" atoms caused by the removal of one of the carbon atoms from hexagon structure of the nanotubes under electron bombardment. The free atom on a surface of the formed stable structure attaches to the neighboring pentagon structure and becomes meta-stable. As a result, carbon-carbon bond is broken and pentagon structure is destroyed. The cross section of displacement creation by 30 keV electron beam was estimated to be 2×10^{-18} cm^2, based on an empirical formula given in previous works [81-82]. Ghopra et al. have observed the collapsing of CNs under 800 keV electron irradiation [83]. Studies have suggested that an accelerating voltage lower than 300 keV does not create significant damage [83-85]. In our studies dimensional changes developed at a much lower value of the accelerating voltage (30 keV).

The maximum energy transferred to carbon atoms in a head-on collision with 30 keV electron beam was calculated to be 5.48 eV. This value is much lower than displacement energy of graphite (20 eV), which indicates that binding energy of carbon atoms in carbon nanotubes is much lower than the binding energy of bulk materials. Based on this, the two following mechanisms are thought to be responsible for dimensional changes of carbon nanotubes under electron beam: a) electron excitation that causes self-organization of the bonds and b) reduced binding energy of the material under high stress. Further studies are needed to reveal the details.

To study impact of ion beam on CNs in microscopes, MWNTs were bombarded by 30 keV Ga ions and in situ characterized by using both SEM and FIB imaging. The shaded square area in the center of Fig. 17 refers to the region selected for ion irradiation. The area of this region was 100×100 um^2. The current of the focused Ga ion beam during irradiation was minimized to be around 260 pA. The whole ion irradiation experiment continued two and a half hours. The selected region experienced ion irradiation to a fluence of 1.4×10^{17} cm^{-2}.

Fig. 17. SE image illustrating the area irradiated by 30 keV Ga ions at minimized ion current.

Figure 18 shows SE images of MWNTs bombarded with 30 keV Ga ions in FIB. CNs bending was observed within the first five minutes of ion bombardment. The subsequent changes such as collapsing of MWNTs were noticed after 14 minutes of

irradiation which is equivalent to a fluence of 1.3×10^{16} cm^{-2}, and complete collapse of the bombarded MWNT's was observed after 30 minutes, equivalent to a fluence of 2.9×10^{16} cm^{-2}. The arrows in Fig. 18 reveal dimensional changes with increasing irradiation time. The total irradiation dosage corresponding to each image was calculated to be 2.3×10^{14} cm^{-2}. The time required to take one SEM micrograph was ~15 sec.
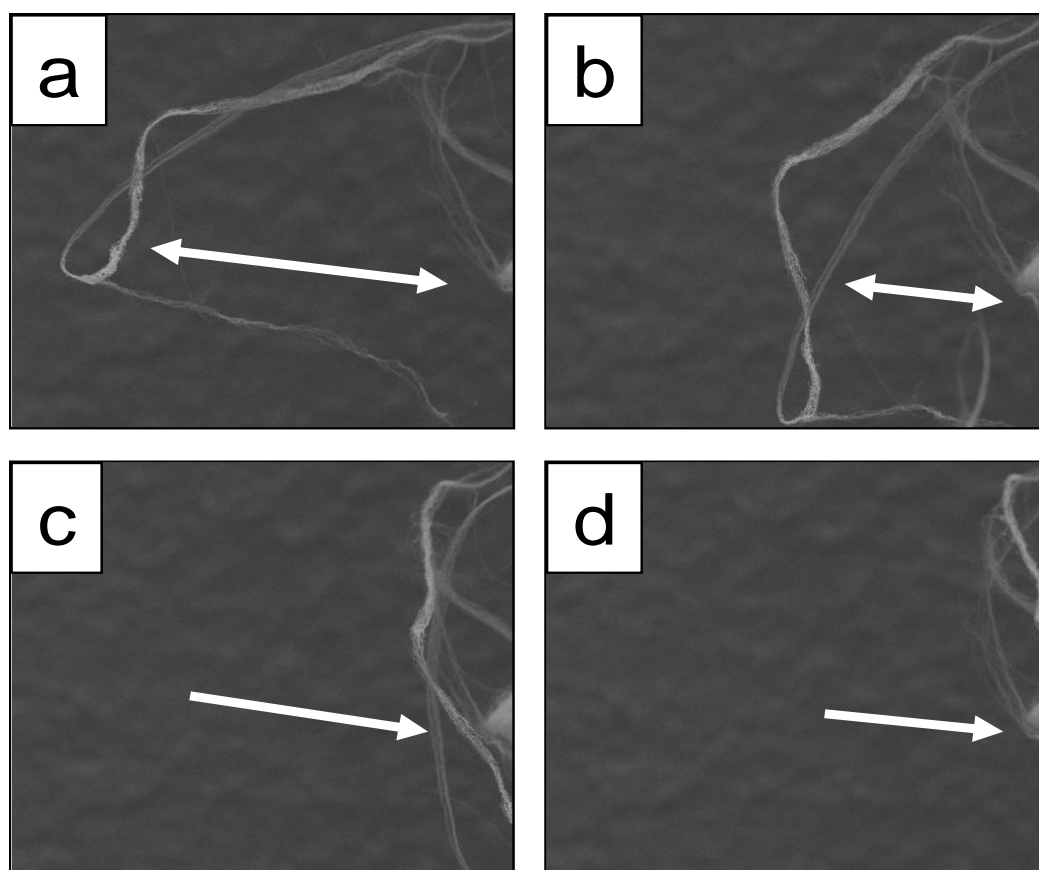
Fig. 18. SE images of MWNTs obtained by irradiating with 30 keV Ga ions in FIB microscope: a) image obtained after t=1 min, b) after t=14 min, c) after t=22 min, and d) after t=28 min of ion bombardment.

Degradation of MWNTs under ion irradiation was expected to be more significant in comparison to the electron irradiation. This can be explained by the fact that cross-section of gallium-carbon interaction is supposed to be larger than electron-carbon interaction cross-section, and by the number of displacements per atom (dpa) Ga ions create in CNs. A displacement cross section for an interaction of Ga ions with CNs was estimated to be 2.5×10^{-15} cm^2 by using Kinchin-Pease model [see Chapter II and Ref. 66]. Based on the studies of Banhart et al., it can be assumed that MWNTs and graphite have similar irradiation hardness [78]. It is not clear at this stage whether vicinity of defects to the free surface of MWNTs can enhance CNs radiation tolerance since the free surface can be a perfect sink for defects. Further studies will be conducted to reveal the details.

6.2. Raman Spectroscopy Study of Irradiated CNs

Irradiation with different ion species, flux and temperatures and post irradiation annealing experiments are able to extract kinetics of interstitial and vacancy migration energies, and energy barrier for defect recombination. To study irradiation damage formation and defect annealing in carbon buckypapers (CBPs), 3 MeV hydrogen (H) and 140 keV helium (He) ion beams were used to irradiate the samples at room temperature, and Raman spectroscopy technique was used to characterize produced damage. According to the Stopping and Range of Ion in Matter (SRIM) simulation [86], penetration depth of 3 MeV H in carbon buckypaper with a density of 0.5 g/cm^3 is 330 micrometers, which indicates that most protons penetrate through the sample of

100 micrometer thickness. In the case of 140 keV He, projected range is calculated to be around 4.3 micrometers. Annealing of the samples was carried in a vacuum furnace at four different temperatures in the range between 500 – 850 ^{o}C.

Figures 19-a and 19-b show secondary electron images of the samples before and after irradiation to a fluence of 3×10^{16} cm^{-2} with 3 MeV H. Networking of randomly distributed MWNTs is visible. There were no noticeable topography changes of the sample surfaces. Our previous study has demonstrated that electrical resistivity of MWNTs under H irradiation increases with increasing fluence due to enhanced carrier scattering from defects [87].
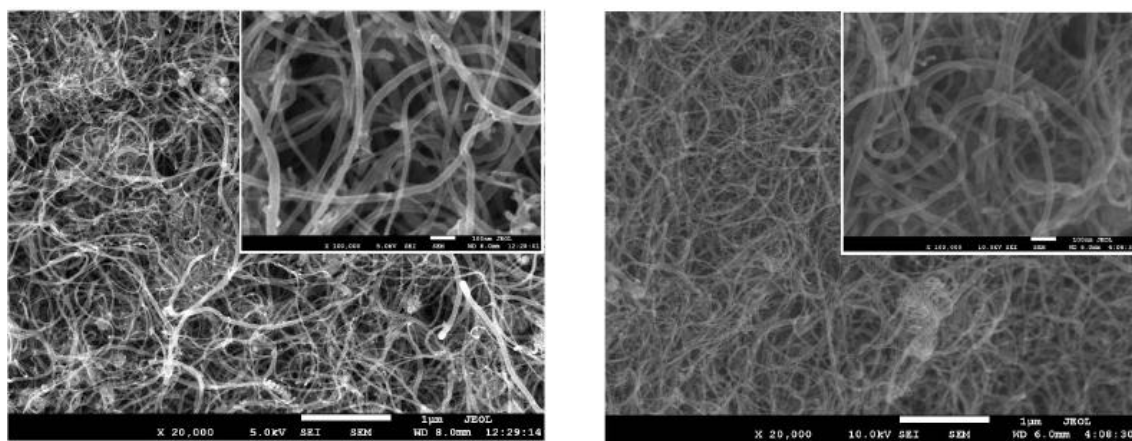

Fig. 19. SE images of the buckypapers (a) before and (b) after 3 MeV H ion irradiation to a fluence of 3×10^{16} cm^{-2}.

Figures 20-a and 20-b show Raman spectra of buckypapers after 140 keV He, and 3 MeV H ion irradiation, respectively. All spectra have features with several

characteristic bands. Among them, the D band positioned at 1340 cm^{-1} is related to disorder. It is known that D band is absent in defect free graphite materials. The G band, inclined at 1580 cm^{-1}, is an indication of metallic or semiconductor properties. The mode disposed at 2660 cm^{-1} is recognized as D* band [88].

According to the studies of Skákalová et al., intensity of D* band of SWNTs does not change with defect concentrations under Ar irradiation. Thus, it was argued that D* mode does not involve defects [89]. As shown in Fig. 20-a, the intensity of D* mode decreases with increasing ion fluence. In addition, small but similar trend was observed for G band. Early studies of Compagnini et al., suggested that G band is a combination of a silent B_{2g} motion and Raman-active E_{2g} mode (G mode) [90]. Observations support this interpretation, and suggest that D* and G bands are related.

Figure 21 shows the Raman spectra of the sample before and after 140 keV He irradiation to a fluence of 1×10^{15}cm^{-2}. The comparison clearly shows the enhancement of intensity of D mode and reduction of intensities of both G and D* modes upon ion irradiation. The ratio of intensities of the G to D bands (I_D/I_G) is frequently used to measure the degree of disorder in graphite [88].
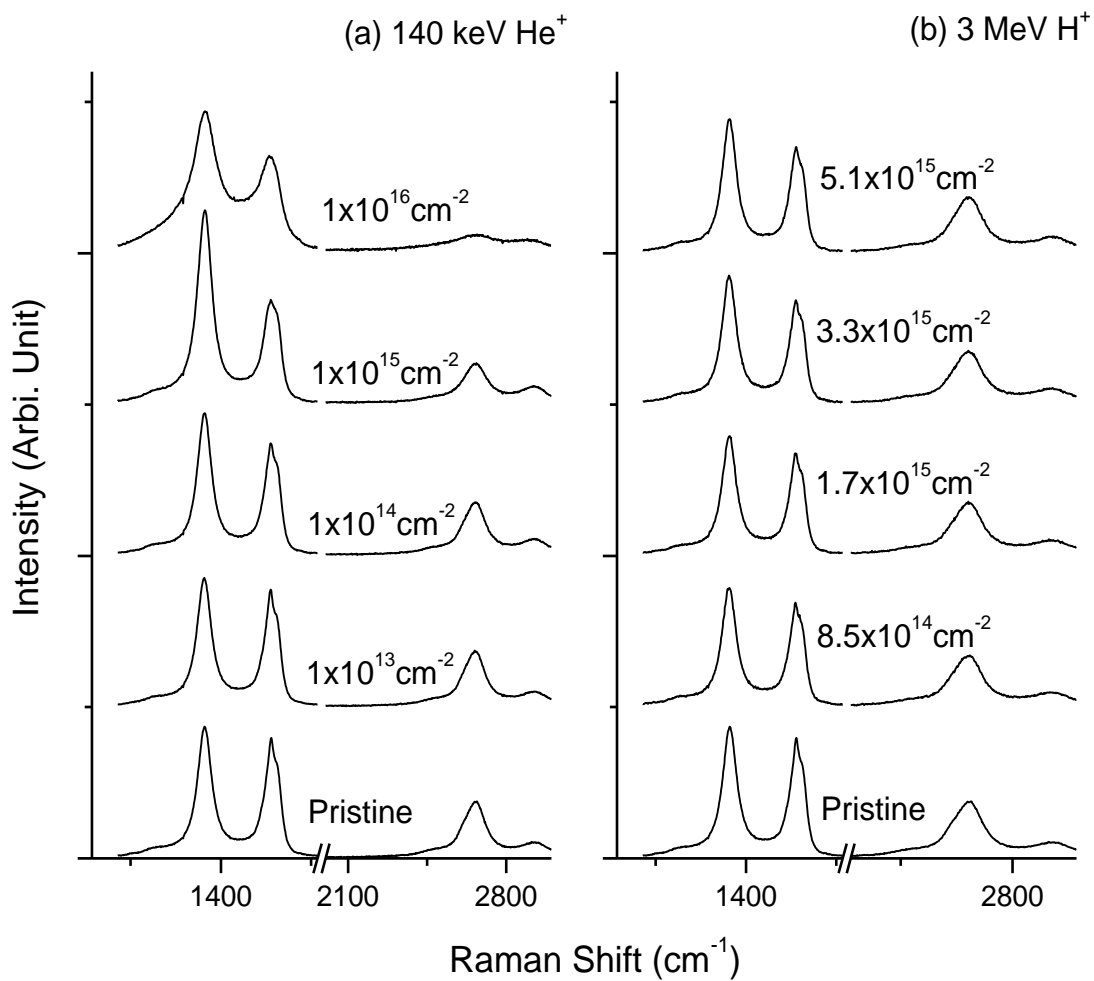
Fig. 20. Raman spectra of carbon buckypapers as a function of fluence for (a) 140 keV He ion irradiation and (b) 3 MeV H ion irradiation.
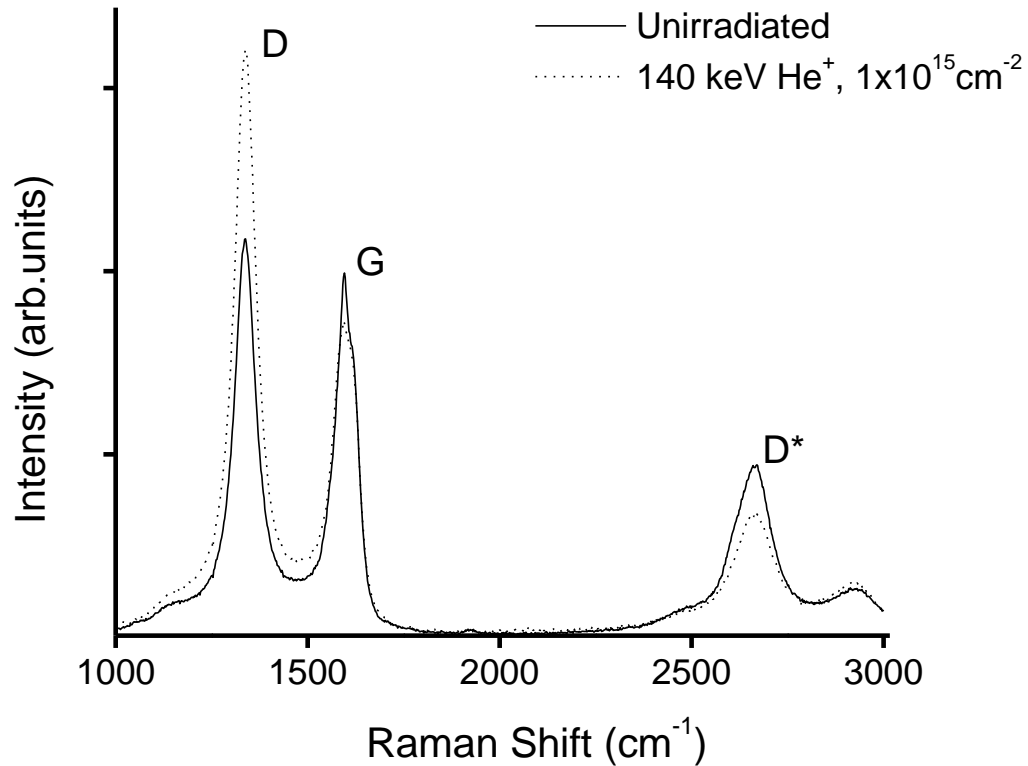
Fig. 21. Raman spectra of carbon buckypaper before and after 140 keV He ion irradiation to a fluence of 1×10^{15} cm^{-2}.

Figures 22-a and 22-b plot the full width at half maximum (FWHM) of G bands as a function of intensities ratio I_D/I_G for both 140 keV He and 3 MeV H irradiated samples, respectively. The arrows guide from the low fluence values to the higher fluence values in a sequence. As shown in Fig. 22-a, FWHM of G band and I_D/I_G ratio remain in a linear relationship for samples irradiated to fluences of 1×10^{13}, 1×10^{14}, and 1×10^{15} cm^{-2}. However, for samples with irradiation fluence above 1×10^{15} cm^{-2} deviation

from the linear trend is obvious. In comparison, Fig. 22-b shows that in case of 3 MeV H irradiation, at all fluence values FWHM has no sudden changes. Early studies have authenticated a linear relationship between FWHM of G bands and intensities ratio of D band to G band (I_D/I_G) [91]. Any deviation from the linear relationship suggests offset of amorphization [91-92]. Based on this criteria, for 140 keV He ion irradiation, it can be concluded that amorphization starts at the fluence values above 1×10^{15} cm^{-2}. For 3 MeV H irradiated samples, the highest fluence of 5.1×10^{15} cm^{-2} does not cause amorphization.

Figure 23 shows intensities ratio I_D/I_G as a function of increasing fluence for 140 keV He and 3 MeV H irradiated samples, respectively. The linear relationship between I_D/I_G ratio and increasing irradiation fluence was noticed in the case of 3 MeV H irradiated sample, and 140 keV He irradiated sample with irradiation fluences below fluence values at which amorphization was noticed. This linear relationship suggests that I_D/I_G ratio represents amount of produced radiation damage. Since stopping power for He in buckypaper is higher than that of H, the larger slope of the curve for He irradiation is expected. The significance of linear relationship is the buildup of damage without considerable dynamic annealing. Otherwise, if mutual recombination becomes significant, defect concentration and equivalently I_D/I_G can reach saturation.
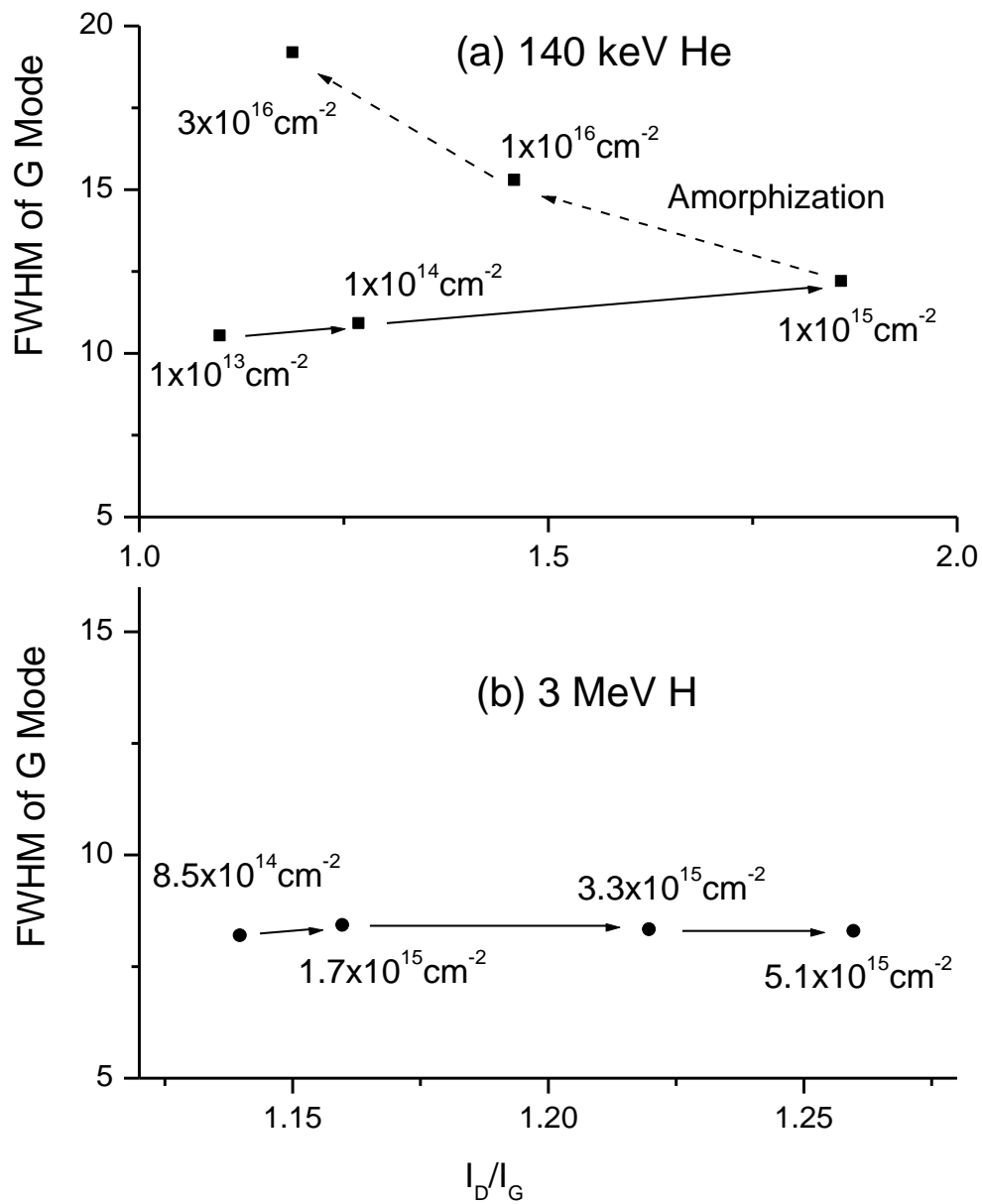
Fig. 22. Full width at half maximum of G band versus intensities ratio of D to G modes I_D/I_G for (a) 140 keV He ion irradiation and (b) 3 MeV H ion irradiation. The arrows point to higher fluences in sequence.
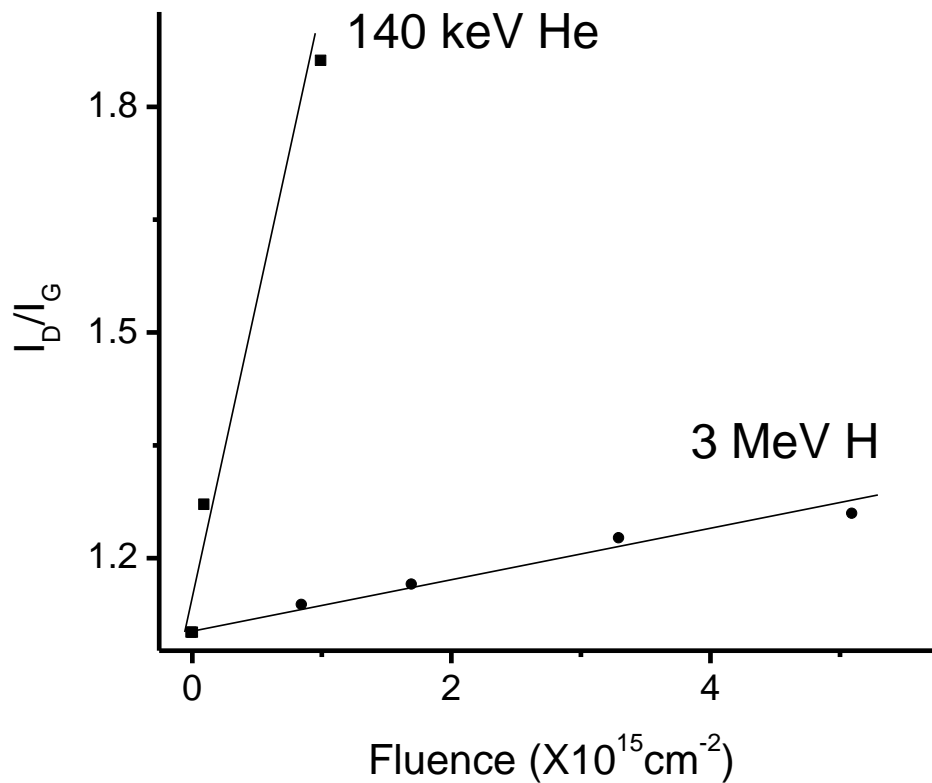
Fig. 23. Intensities ratio of D to G bands I_D/I_G as a function of increasing fluence for 140 keV He and 3 MeV H ion irradiation.

Tuinstra and Koenig suggested that I_D/I_G is inversely proportional to the in-plane crystallite size in single crystal graphite [88]. Later, Nakamura and Kitajima explained changes of I_D/I_G in terms of the reduction in phonon correlation length because of increased defect density [93]. Niwase et al. suggested that intensity ratio I_D/I_G is related to in-plane defects such as single vacancies and vacancy clusters [94]. In a later study conducted by Compagnini et al., it was pointed out that ion irradiation induced $sp^2 \rightarrow sp^3$

transition can also increase intensity ratio [90]. They further assumed coexistence of two different sublattices in irradiated graphite. One is a regular graphite sublattice and another is a cubic diamond like sublattice with sp^3 formation. Each of them has a characteristic line in Raman spectra: G band for graphite lattices, and D band for diamond like sublattices.

Different from single crystalline graphite in which all carbon bonding are sp^2, pristine CNs could have sp^3 bonding because of the tube's curvature. Therefore, it is not surprising to observe a non-zero D bond in Raman spectra of pristine CNs (as shown in Fig. 20-a and 20-b). Upon ion irradiation, momentum transfer from incident particle will cause atomic displacements and creation of interstitial and vacancy pairs, and energy deposition will lead to the inter-wall coupling [91, 95-97]. All these structural changes can cause $sp^2 \rightarrow sp^3$ transition. With increasing ion fluence, defect density and bond transition are increasing, leading to the higher values of I_D/I_G ratio. When defect densities reach a certain value, density of phonon states between diamond like lattice and graphite sublattice become so high that scattering occurs in the region between D and G bands [90]. This corresponds to the high fluence irradiation such as the ones above 1×10^{15}cm^{-2} for 140 keV He irradiation.

Figure 24 shows the change of I_D/I_G ratio for the sample irradiated to a fluence of 1.7×10^{15} cm^{-2} with 3 MeV H, and annealed at various temperatures for 15 minutes. The I_D/I_G ratio values were calculated to be: 1.16 for irradiated but not annealed sample, 1.10 for the sample annealed at 600 ^{o}C, 1.08 annealed at 675 ^{o}C, 1.03 annealed at 750 ^{o}C, and 1.01 annealed at 825 ^{o}C. Since the value of I_D/I_G ratio is linearly proportional to the

radiation damage, reduction of the values of I_D/I_G ratios is caused by defect annealing. The data is fitted by an Arrhenius curve which gives activation energy of 0.36±0.05 eV.
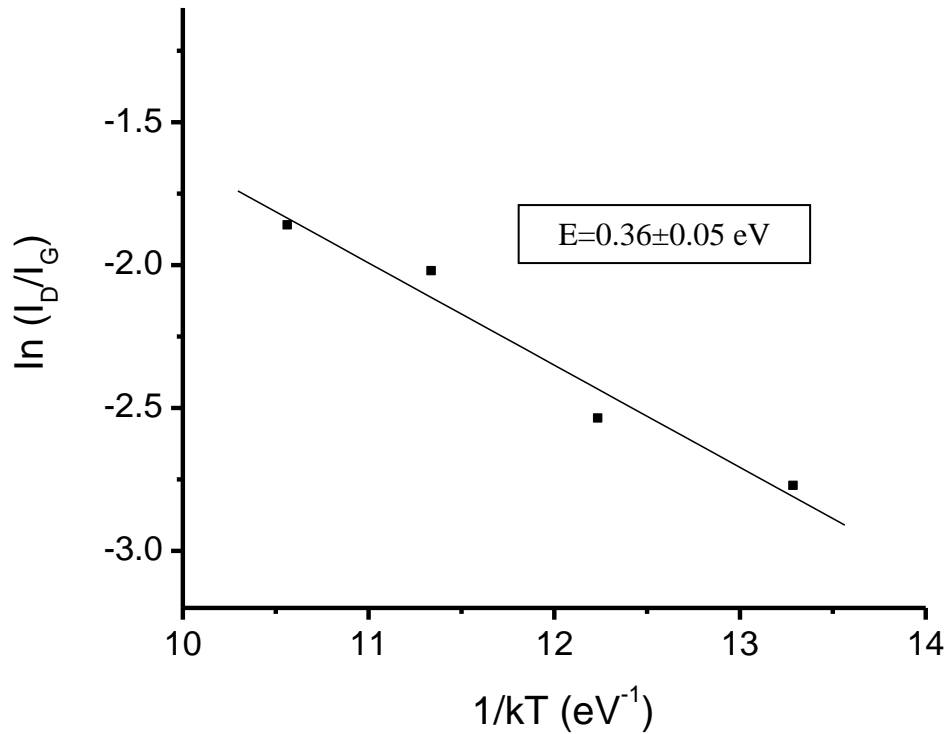

Fig. 24. Intensities ratio of D to G modes I_D/I_G as a function of annealing temperature for the buckypaper irradiated with 3 MeV H to a fluence of 1×10^{15} cm^{-2}.

Previous studies suggested that vacancies which have migration energy of ~3eV, are almost immobile in graphite, while interstitials are highly mobile with migration energy less than 0.1 eV [24]. It is a general consensus that migration and formation energy of point defects in CNs is different from graphite because of the curvature of

nanotube. Atomic scale modeling by Krasheninnikov et al. exhibited migration energy of 0.5 - 0.7 eV for C atoms in single wall carbon nanotubes with diameters of 1-1.4 nm. Migration energy was found to be weakly dependent on the diameter of nanotubes [98]. Displaced C atoms can either diffuse on the outside surface of nanotubes as adatoms, or diffuse on the inner surface of nanotubes as interstitials. Interstitials diffusion has lower migration energy than migration energy of adatoms. Interstitial can also penetrate the shell, but this requires a much higher energy barrier [78].

Extracted activation energy for defect annealing was close to the modeling value which has predicted migration energy of C interstitials (0.5 eV for CNs with large diameter) [98]. However, it is difficult to define physical meaning of this energy, since potential barrier for interstitial-vacancy recombination is not known. This energy can also be explained as the activation energy for $sp^2 \rightarrow sp^3$ transition. Further studies are needed to explain the physical meaning of the extracted activation energy.

Figure 25 shows intensities ratio of D to G bands (I_D/I_G) as a function of post-irradiation annealing temperatures for the sample irradiated with 140 keV He ions to a fluence of 3×10^{16} cm^{-2}. According to previous discussion (Fig. 22-a), this fluence is high enough to induce amorphization which involves the formation of significant three dimensional defects such as cavities surrounded by interstitial atoms and clusters of sp^3 bonds. These defects are difficult to remove. As it can be observed, the I_D/I_G ratios' value is almost constant except at high temperature of 850 ^{o}C where it increases. This agrees with early observations of graphite where annealing of amorphized graphite at high temperature increased I_D/I_G value [92].
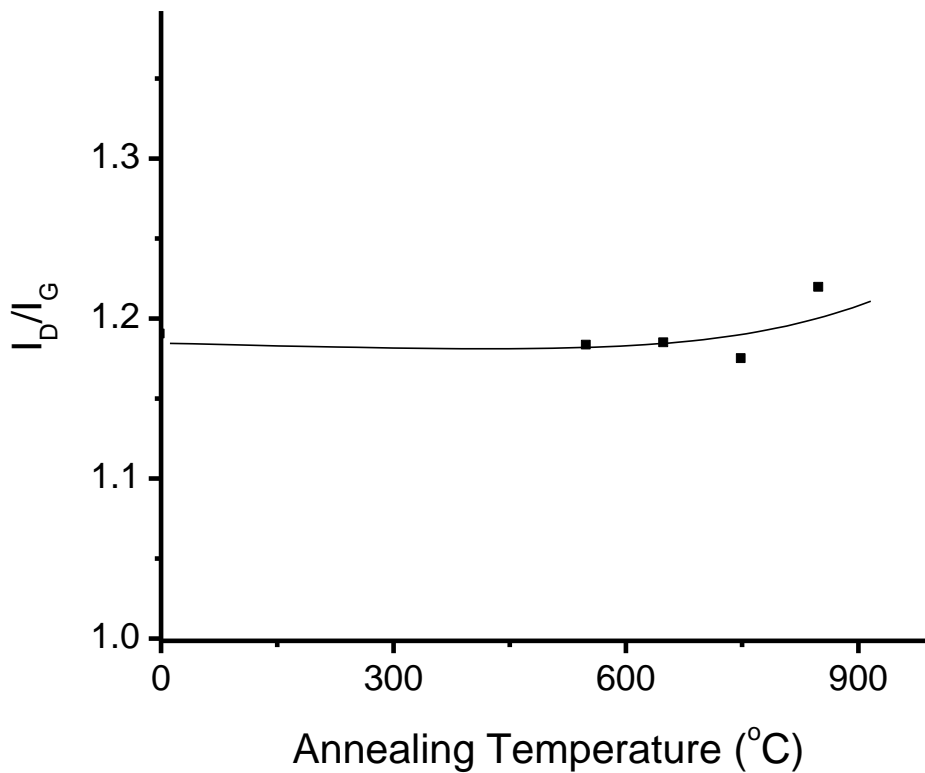
Fig. 25. I_D/I_G ratio as a function of annealing temperature for buckypaper irradiated with 140 keV He to a fluence of 3×10^{16} cm^{-2}.

It can be concluded from the discussion above, for self-supporting carbon buckypapers irradiated with 140 keV He and 3 MeV H ions to different fluences, intensity ratio of D to G bands I_D/I_G increases linearly with increasing fluence. Annealing of irradiated samples was found to reduce the intensities ratio, and suggests a defect removal process with activation energy of 0.36±0.05 eV. Defect annealing becomes difficult for the heavily damaged samples.

6.3. Proton Irradiation of CNs and in situ Resistivity Measurements

Damage morphology is different for various ion species. Bombardment of carbon nanotubes to different fluxes and energies with light ions such as H and He, and heavy ions such as Ar is needed to investigate ability of CNs to repair light damage containing mainly separated Frenkel pairs or heavy damage with damage cascade formation. This section will be focused on irradiation stability of carbon nanotubes under proton beam. As possible type of materials that can be used in an outer space, carbon nanotubes should be exposed to proton irradiation to test their stability in harsh environment. The main point of using proton beam is the fact that protons are important components in radiation belts about planets such as Earth, Jupiter, etc. Another reason of preferring to use proton beam is penetration depth of protons in carbon buckypapers which is much higher than for other ion species.

In previous studies, such as TEM study of the morphological changes of 3 MeV proton irradiated single-walled carbon nanotubes', radiation stability and welding of nanotubes irradiated to low doses, amorphization, loss of nanotubes physical integrity and production of radiation damage in nanotubes irradiated to higher doses was reported [99]. Khare et al. showed that SWNT film becomes transparent after irradiation with 1 MeV H beam. Raman analysis gave a clear evidence of formation of C-H bonds in irradiated samples. This result points out one of the future possibilities of using proton irradiation as a tool to achieve atomic hydrogen functionalizaiton of carbon nanotubes which can be subsequently used as a shielding material [100].

To reveal the damage formation mechanism in carbon buckypapers under a high-energy proton irradiation, 2 MeV H beam was used to irradiate carbon buckypapers and characterization of resistivity changes as a function of time was done in situ. Electric resistivity measurements are proportional to the population of defects, so measuring electric resistivity provides capability of in situ defect characterization during irradiation.

Advantages of measuring resistivity in situ during irradiation for defect characterization are:

    a) Damage buildup and dynamic annealing of defects can be revealed.

    b) Stability of CNs in harsh environments can be evaluated since electrical resistivity changes directly reveal the scattering of electrons by radiation damage.

Schematic representation of the expected resistivity changes as a function of increasing irradiation time is given in Fig. 26. The detailed discussion on the stages of damage production can be found in Chapter II.

The total fluence of protons was selected to be 7×10^{15} cm^{-2}, and different beam currents of 200, 100 and 50 nA were used to achieve the desired fluence. The corresponding values of the flux were as follows: 1.18×10^{11} cm^{-2}*sec^{-1}, 9.86×10^{11} cm^{-2}*sec^{-1} and 1.97×10^{12} cm^{-2}*sec^{-1}, respectively. According to the SRIM simulation [86], the penetration depth of 2 MeV H in carbon buckypaper with a density of 0.5 g/cm^3 is 170 micrometers, which indicates that most protons penetrate through the sample of 100 micrometer thickness.
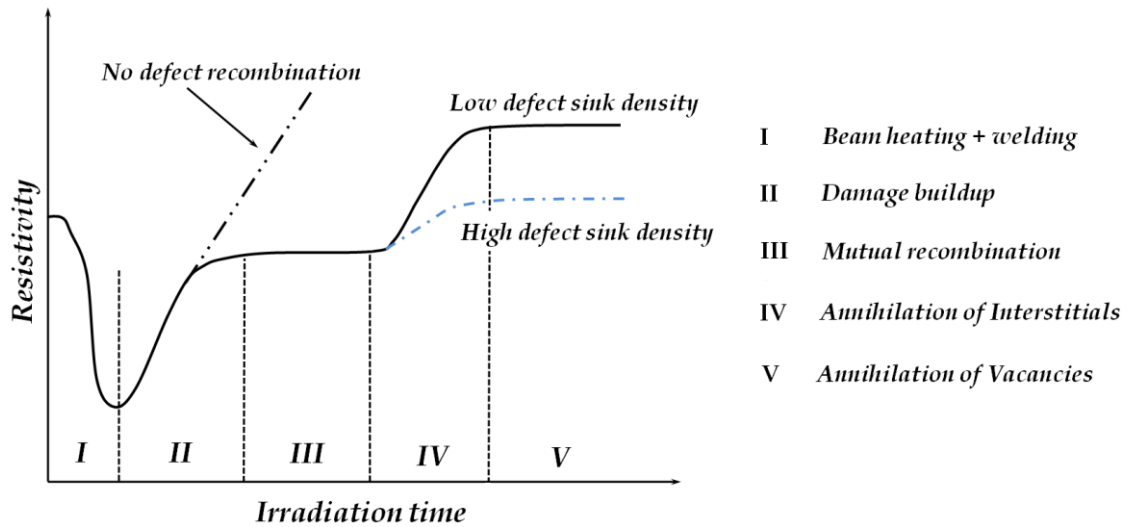
**Fig. 26**. Schematic representation of resistivity changes of MWNTs as a function of irradiation fluence.

Figure 27 shows SE images of carbon buckypapers prior and after 2 MeV proton irradiation to a total fluence of 7×10^{15} cm^{-2}, with the flux of 1.9×10^{12} cm^{-2}*sec^{-1}. Figures 27-a and 27-c show SE images of the carbon buckypapers prior to irradiation collected at different magnification values. Figures 27-b and 27-d show SE images of the carbon buckypapers damaged under ion beam, acquired at various magnification values.

Figure 28 shows resistance vs. time for 2 MeV H irradiated buckypaper to the flux values of 1.18×10^{11} cm^{-2}*sec^{-1}, 9.86×10^{11} cm^{-2}*sec^{-1} and 1.97×10^{12} cm^{-2}*sec^{-1}. The resistance was normalized to the value before ion irradiation. As shown in Fig. 28-a, once the beam was turned on, resistance instantly decreased (phase I), then increased (phase II) and saturated (phase II). At the end of irradiation period, resistance rose to a

higher value (phase IV). Similar trend can be observed in case of lower flux values , once the beam was turned on, resistance decreased at first (phase I), remained relatively stable (phase II), and at the end of irradiation period rose to a higher value (phase III). Refer to Fig. 28-b and 28-c during description of the resistivity changes as a function of increasing irradiation time.
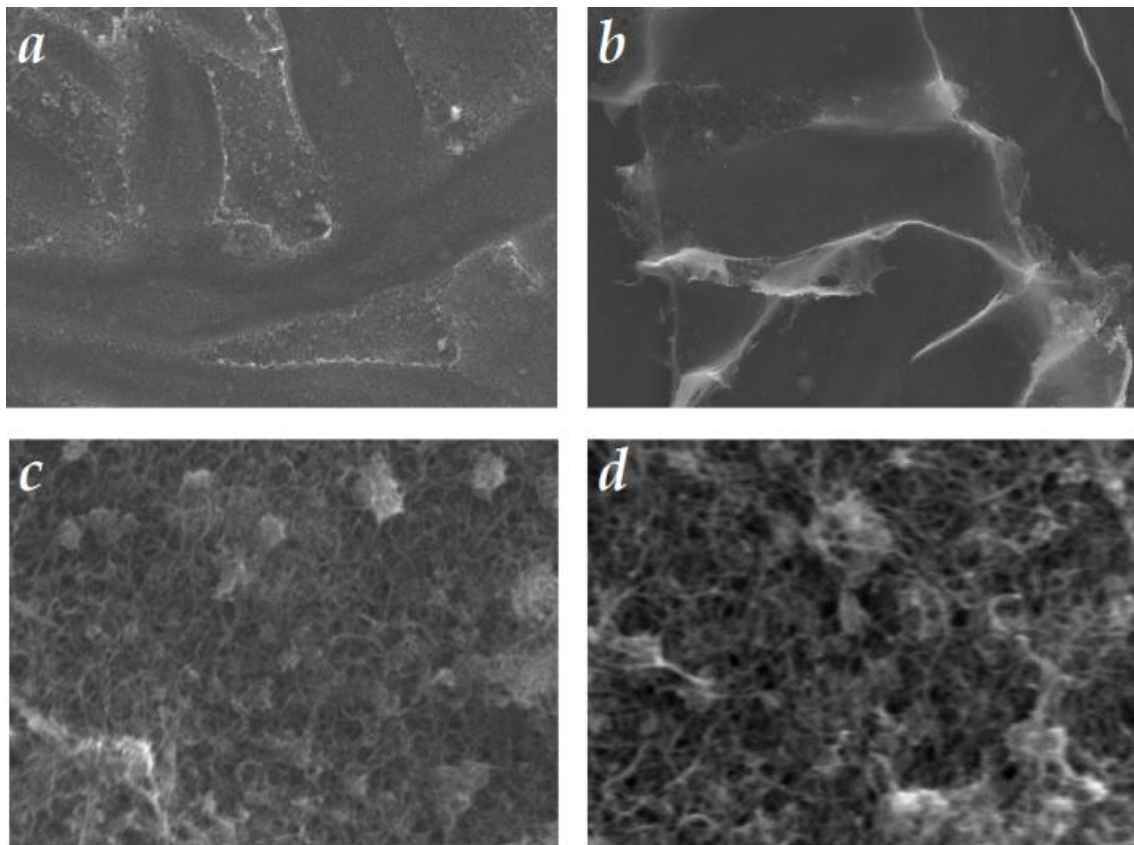
**Fig. 27**. SE images of buckypapers: a) and c) Prior to irradiation with markers denoting 35 um and 3 um, respectively, b) and d) after irradiation to a total fluence of 7×10^{15} cm^{-2} with markers denoting 35 um and 3 um, respectively.
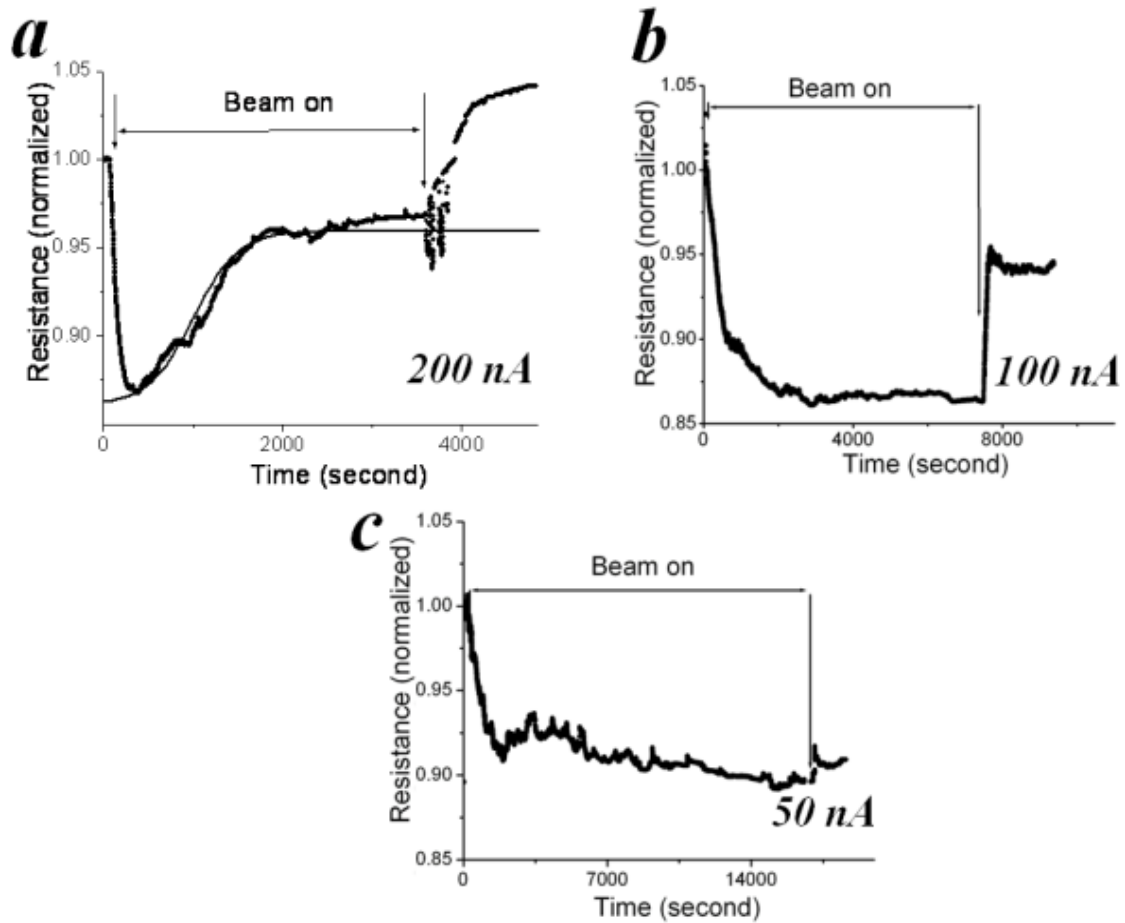
Fig. 28. Resistance changes vs. irradiation time for carbon buckypapers irradiated to the flux values of: a) 1.97×10^{12} cm^{-2}*sec^{-1}, b) 9.86×10^{11} cm^{-2}*sec^{-1} and c) 1.18×10^{11} cm^{-2}*sec^{-1}.

Figure 29 shows Raman spectra of buckypapers after 2 MeV H ion irradiation to the flux values of 4.7×10^{11} cm^{-2}*sec^{-1}, 7.6×10^{11} cm^{-2}*sec^{-1} and 1.3×10^{12} cm^{-2}*sec^{-1}. The spectra has features, with several characteristic modes that includes disorder band (D band), positioned at 1340 cm^{-1}, G band which is a combination of B_{2g} motion and the Raman-active E_{2g}, positioned at 1592 cm^{-1}, and D* band disposed at 2660 cm^{-1}. Upon irradiation under different beam currents, positions of D, G, and D* bands shifted from

initial values. The intensity of D^* mode, as in cases of 3 MeV H and 140 keV He ions bombardment decreased with increasing flux value.
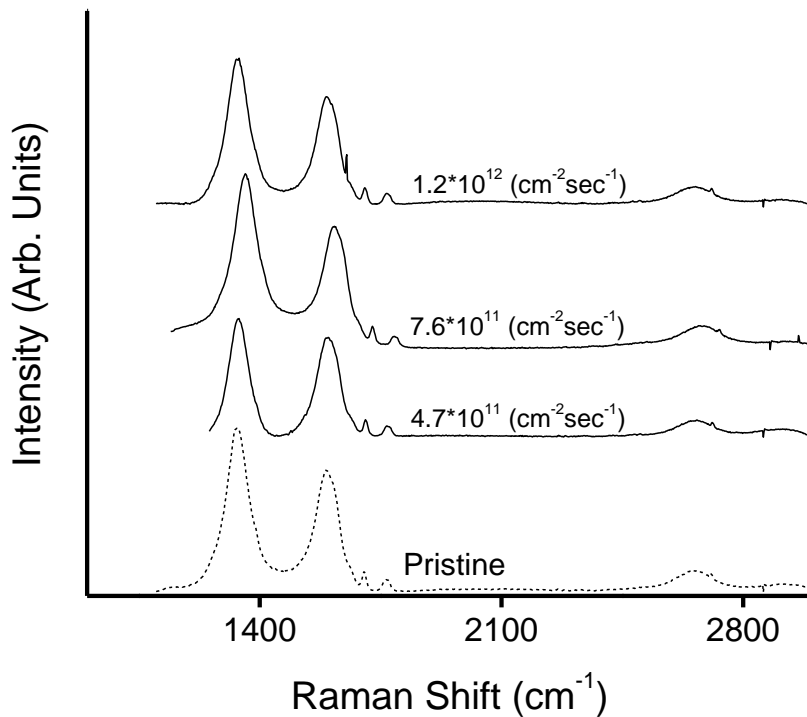
Fig. 29. Raman spectra of carbon buckypapers irradiated to a fluence of 7×10^{15} cm^{-2} and flux values of 4.7×10^{11} cm^{-2}*sec^{-1}, 7.6×10^{11} cm^{-2}*sec^{-1} and 1.3×10^{12} cm^{-2}*sec^{-1}.

Figure 30 shows the typical time dependent changes of the temperature of buckypapers under 2 MeV H irradiation. The temperature increased linearly at the early stage of irradiation, and remained relatively stable until the end of irradiation period. Once the beam was turned off, temperature decreased. The temperature behavior was in

agreement with resistivity changes shown in Fig. 28. The temperature behavior mentioned above was similar in all three cases, thus accurate control of experimental conditions can be suggested. However, other mechanisms such as welding of carbon nanotube network can affect the resistance changes and temperature might play a secondary role. Further studies are needed to reveal the details.
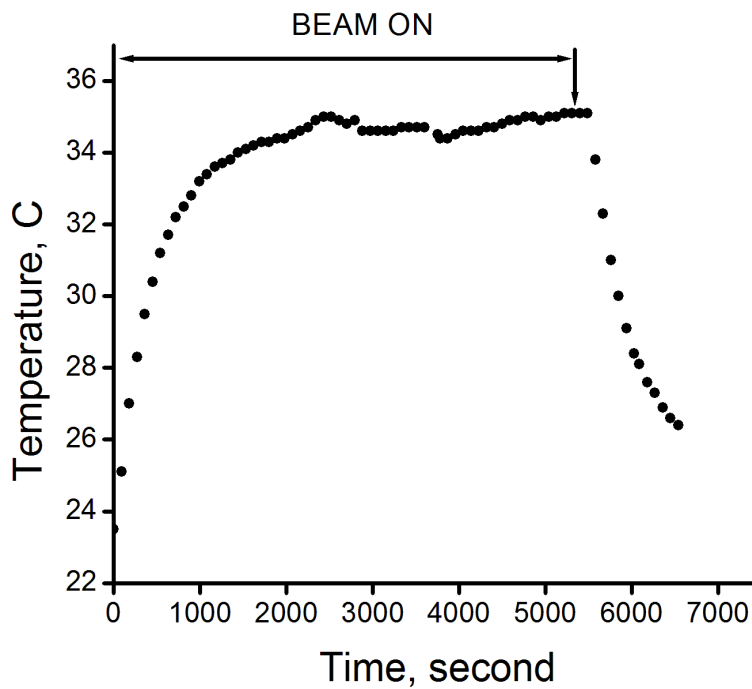
Fig. 30. The change of the temperature with increasing irradiation time.

Raman scattering technique, widely used for identification of defects in carbon nanotubes [101-103] demonstrated production of defects upon irradiation of

buckypapers. In accordance with observations, not only D but also G bands were influenced by irradiation. The ratio of intensities of D to G modes (I_D/I_G) denoting defect density and providing an evaluation of the quality of the buckypapers, increased in irradiated samples. This increase indicated production of irradiation induced defects [88, 90-91, 93]. Within calculated error bar, data obtained from the Raman spectra of buckypapers was consistent with the changes of resistance with increasing irradiation time.

In order to explain the changes of resistance with time, defect reaction rate theory will be considered [see Chapter II and Ref. 66]. It is known that resistivity of semiconducting CNs drops with increasing temperature. Therefore, it is believed that phase I was mainly because of the beam heating. Heating, which is presumed to saturate rapidly, can be minimized by abating ion flux. One of the other possible reasons instigating exponential decrease of resistivity is welding of nanotubes. However, since welding typically develops at high temperatures and is not expected to occur under light ion irradiation, beam heating is assumed to be the main explanation of the phenomenon. In case of the higher flux values, phase II was primarily because of the defect creation under ion bombardment. As it was discussed in Chapter II and shown in Fig. 26, and 28, defect concentrations build up linearly at first. However, with increasing number of defects, carrier scattering becomes significant and resistivity increase is expected in the next phase. Phase III suggests the achieved balance between defect creation and annealing. In phase IV, resistivity enhancement was because of the sample cooling when the beam was off.

Under the consideration that defect creation and recombination rates are in a balance, evolution of phase II to III can be modeled. For interstitial defects, its time dependent changes given by Eq. (3.7), were derived in previous chapter. This equation leads to the solution, which was used to model the transformation of the phase II into the phase III. The solid line in Fig. 28-a is a fitted curve from Equation (3.17). Good agreement suggests that in a carbon buckypaper, a quasi steady state of defect creation and dynamic defect annealing exists.

In the cases with lower flux values, phase I is believed to be principally because of the beam heating. Lower flux values at fixed fluence suggest the slower defect production rate, and require longer irradiation time to exhibit behavior similar to that of a higher beam current. In order to preserve the fluence of $\sim 7 \times 10^{15}$ cm^{-2}, further development of resistivity with time was not observed. However, the changes of resistivity should be consistent with the results obtained for high flux values.

The presence of point defects increases materials' resistivity, and changes of resistivity are approximately linearly proportional to defect densities. As it was proved in discussion, measurements of resistivity can be used as a valuable tool in revealing fundamentals of ion solid interactions in CNs, which shows dynamic defect recombination and role of the surface in defect annealing.

CHAPTER VII

CONCLUSION

This thesis was aimed to study irradiation stability of carbon nanotubes. Different ion species at various energies were chosen to bombard carbon nanotubes and related materials. Several defect characterization techniques were used to study damage formation mechanism in carbon nanotubes.

It has been discovered that dimensional changes of carbon nanotubes in microscopes can develop when operating at accelerating voltages of 30 keV, which indicated that binding energy of carbon atoms in CNs is much lower than in bulk materials. The two possible reasons of dimensional changes of carbon nanotubes observed in experiments were electron excitation which caused self-organization of the bonds, and reduced binding energy of the material under high stress.

In situ resistivity measurements during 2 MeV H irradiation provided by two-point probe set up revealed existence of a quasi state of defect creation. This leads to a conclusion that dynamic defect annealing in carbon buckypapers upon irradiation takes place.

Raman spectroscopy study of 3 MeV H and 140 keV He irradiated carbon buckypapers revealed linear relationship between I_D/I_G ratio and increasing irradiation fluence. This linear relationship did not hold for the samples irradiated to very high fluence values. As it has been shown, annealing of irradiated samples reduced the value of I_D/I_G ratio and removed defects. However, in amorphized samples kinetic energy for

defect removal was high, and annealing was not able to affect I_D/I_G ratio and remove defects. The value of extracted activation energy for the sample irradiated with 3 MeV H to a dose of $1.7x10^{15}$ cm^{-2} was found to be 0.36 ± 0.05 eV, which means existence of a faster diffuser (interstitial). The value of activation energy was in good agreement with theoretical studies.

REFERENCES

[1] S. Iijima, Nature 354 (1991) 56.

[2] A. Oberlin, M. Endo, and T. Koyama, J. Cryst. Growth. 32 (1976) 335.

[3] M. S. Dresselhaus, G. Dresselhaus, and P. Avouris (Eds), Carbon Nanotubes: Synthesis, Structure, Properties and Applications, Springer, Berlin, 2001.

[4] R. H. Baughman, A. A. Zakhidov, and W. A. de Heer, Science 297 (2002) 787.

[5] A. V. Krasheninnikov and F. Banhart, Nat. Mater. 6 (2007) 723.

[6] Z. Yao, C. L. Kane and C. Dekker, Phys. Rev. Lett. 84 (2000) 2941.

[7] M. Fujii, X. Zhang, H. Xie, H. Ago, K. Takahashi, T. Ikuta, H. Abe, T. Shimizu, Phys. Rev. Lett. 95 (2005) 065502.

[8] E. W. Wong, P. E. Sheehan, C. M. Lieber, Science 277 (1997) 1971.

[9] M. M. Treacy, T. W. Ebbesen, J. M. Gibson, Nature 381 (1996) 678.

[10] L. Sun, A.V. Krasheninnikov, T. Ahlgren, K. Nordlund, and F. Banhart, Phys. Rev. Lett. 101 (2008) 156101.

[11] L. Sun, F. Banhart, A.V. Krasheninnikov, J.A. Rodriguez-Manzo, M. Terrones and P.M. Ajayan, Science 312 (2006) 1199.

[12] A. Kis, G. Csányi, J.-P. Salvetat, T.-N. Lee, E. Couteau, A. J. Kulik, W. Benoit, J. Brugger and L. Forró, Nat. Mater. 3 (2004) 153.

[13] A. Busnaina, Nanomanufacturing Handbook, CRC Press, Boca Raton, 2007.

[14] J. A. Åström, A. V. Krasheninnikov, and K. Nordlund, Phys.Rev. Lett. 93 (2004) 215503.

[15] F. Banhart, J.X. Li and M. Terrones, Small 1 (2005) 953.

[16] J. X. Li and F. Banhart, Nano Lett. 4 (2004) 1143.

[17] A. Krasheninnikov, "Irradiation-induced phenomena in carbon nanotubes", in: V. A. Basiuk, E. A. Basiuk (Eds.), "Chemistry of Carbon Nanotubes", American Scientific Publishers, California, 2007.

[18] A. Hashimoto, K. Suenaga, A. Gloter, K. Urita, and S. Iijima, Nature 430 (2004) 870.

[19] K. Urita, K. Suenaga, T. Sugai, H. Shinohara, and S. Iijima, Phys. Rev.Lett. 94 (2005) 155502.

[20] C. P. Ewels, R. H. Telling, A. A. El-Barbary, and M. I. Heggie, Phys.Rev. Lett. 91 (2003) 025505.

[21] A. A. El-Barbary, R. H. Telling, C. P. Ewels, M. I. Heggie, and P. R. Briddon, Phys. Rev. B 68 (2003) 144107.

[22] R. Telling, C. Ewels, A. El-Barbary, and M. Heggie, Nat. Mater. 2 (2003) 333.

[23] A. V. Krasheninnikov, P. O. Lehtinen, A. S. Foster, and R. M. Nieminen, Chem. Phys. Lett. 418 (2006) 132.

[24] P. A. Thrower and R. M. Mayer, Phys. Stat. Sol. (a) 47 (1978) 11.

[25] K. Thompson, M.S. thesis, Texas A&M University, 1994.

[26] J. J. Carter, M.S. thesis, Texas A&M University, 2006.

[27] E. Smith, G. Dent, Modern Raman Spectroscopy – A Practical Approach, John Wiley & Sons, New York, 2005.

[28] G. Gouadec, P. Colomban, Prog. Cryst. Growth Charact. Mater. 53 (2007) 1.

[29] J. J. Bozzola, L. D. Russell, Electron Microscopy, Jones and Bartlett Publishers, Boston, 1999.

[30] V. N. Popov, Mater. Sci. Eng. R 43 (2004) 61.

[31] M. Paradise, T. Goswami, Mater. Design 28 (2007) 1477.

[32] Y. Homma, Y. Kobayashi, T. O. Takagi, R. I. Y. J. Jung, P. M. Ajayan, J. Phys. Chem. B 107 (2003) 12161.

[33] T. W. Ebbesen, P. M. Ajayan, Nature 358 (1992) 220.

[34] D. S. Bethune, C. H. Klang, M. S. de Vries, G. Gorman, R. Savoy, J. Vazquez, R. Beyers, Nature 363 (1993) 605.

[35] C. Journet, W. K. Maser, P. Bernier, A. Loiseau, M. Lamy de la Chapelle, S. Lefrant, P. Deniard, R. Lee, J. E. Fischer, Nature 388 (1997) 756.

[36] C. J. Lee, J. Park, J. M. Kim, J. Y. Lee, Y. Huh, K. S. No, Chem. Phys. Lett. 327 (2000) 277.

[37] S. Xie, W. Li, Z. Pan, B. Cahng, L. Sun, Mater. Sci. Eng. A 286 (2000) 11.

[38] C. J. Lee, S. C. Lyu, H. W. Kim, C. Y. Park, C. W. Yang, Chem. Phys. Lett. 359 (2002) 109.

[39] K. Hernadi, Chem. Phys. Lett. 363 (2002) 169.

[40] J. Kong, H. T. Soh, A. M. Cassell, C. F. Quate, H. Dai, Nature 395 (1998) 878.

[41] B. Q. Wei, Z. J. Zhang, G. Ramanath, P. M. Ajayan, Appl. Phys. Lett. 77 (2000) 2985.

[42] J. Kong, N. R. Franklin, C. Zhou, M. G. Chapline, S. Peng, K. Cho, H. Dai, Science 287 (2000) 622.

[43] S. Fan, M. G. Chapline, N. R. Franklin, T. W. Tombler, A. M. Cassell, H. Dai, Science 283 (1999) 512.

[44] A. M. Cassell, J. A. Raymakers, J. Kong, H. Dai, J. Phys. Chem. B 103 (1999) 6484.

[45] I. S. Jung, S. Lee, Y.-H. Song, S.-Y. Choi, K.-I. Cho, K.-S. Nam, Appl. Phys. Lett. 78 (2001) 901.

[46] A. Thess, R. Lee, P. Nikolaev, H. Dai, P. Petit, J. Robert, et al., Science 273 (1996) 483.

[47] W. Z. Li, S. S. Xie, L. X. Qian, B. H. Chang, B. S. Zou, W. Y. Zhou, R. A. Zhao, G. Wang, Science 274 (1996) 1701.

[48] M. Terrones, N. Grobert, J. Olivares, J. P. Zhang, H. Terrones, K. Kordatos, et al., Nature 388 (1997) 52.

[49] Z. F. Ren, Z. P. Huang, J. W. Xu, J. H. Wang, P. Bush, M. P. Siegal, P. N. Provencio, Science 282 (1998) 1105.

[50] B. Q. Wei, R. Vajtai, Y. Jung, R. Zhang, G. Ramanath, P. M. Ajayan, Nature 416 (2002) 495.

[51] Y. Jung, B. Q. Wei, R. Vajtai, J. Ward, R. Zhang, G. Ramanath, P. M. Ajayan, Mat. Res. Soc. Symp. Proc. 706 (2002) Z3.

[52] B. Q. Wei, R. Vajtai, Y. Jung, J. Ward, R. Zhang, G. Ramanath, P. M. Ajayan, Chem. Mater. 15 (2003) 1598.

[53] Y. Jung, B. Wei, R. Vajtai, P. M. Ajayan, Y. Homma, K. Prabhakaran, T. Ogino, Nano Lett. 3 (2003) 561.

[54] Y. Jung, Y. Homma, T. Ogino, Y. Kobayashi, D. Takagi, B. Wei, R. Vajtai, R. M. Ajayan, J. Phys. Chem. B 107 (2003) 6859.

[55] A. K. Sinha, D. W. Hwang, L. P. Hwang, Chem. Phys. Lett. 332 (2000) 455.

[56] J. Kong, A. M. Cassell, H. Dai, Chem. Phys. Lett. 292 (1998) 567.

[57] I. T. Han, H. J. Kim, Y.-Y. Park, N. Lee, J. E. Jang, J. W. Kim, J. E. Jung, J. M. Kim, Appl. Phys. Lett. 81 (2002) 2070.

[58] Y. C. Choi, D. J. Bae, Y. H. Lee, B. S. Lee, G.-S. Park, W. B. Choi, N. S. Lee, J. M. Kim, J. Vac. Sci. Technol. A 18 (2000) 1864.

[59] R. Andrews, D. Jacques, A. M. Rao, F. Deebyshire, D. Qian, X. Fan, E. C. Dickey, J. Chen, Chem. Phys. Lett. 303 (1999) 467.

[60] Z. J. Zhang, B. Q. Wei, G. Ramanath, P. M. Ajayan, Appl. Phys. Lett. 77 (2000) 3764.

[61] T. Guo, A. Thess, D. T. Colbert, R. E. Smalley, Chem. Phys. Lett. 243 (1995) 49.

[62] Preparation of carbon buckypaper, NanoLab's carbon nanotube paper, 15 March 2006, <http://lib.store.yahoo.net/lib/nanolab2000/preparation-of-buckypaper.pdf>.

[63] L. Svarovsky, Solid-Liquid Separation, Butterworth-Heinemann, Oxford, 2000.

[64] M. Nastasi, J. W. Mayer, J. K. Hirvonen, Ion-Solid Interactions: Fundamentals and Applications, Cambridge University Press, Cambridge, 1996.

[65] S.M. Bruemmer, Proceedings of the 10th International Conference on Environmental Degradation of Materials in Nuclear Power Systems: Water Reactors. NACE International, 2002, Houston, TX.

[66] G. Was, Fundamentals of Radiation Material Science: Metals and Alloys, Springer, Berlin, 2007.

[67] T. Yamamoto, Quantum Theory of Thermal Transport in Carbon Nanotubes, The 9th Asian Workshop on First-Principles Electronics Structure Calculations, November 6-8, 2006, Seoul, Korea.

[68] A.V. Krasheninnikov and K. Nordlund, J. Vac. Sci. Technol. B 20 (2002) 728.

[69] N. Kondo, T. Yamamoto, K. Watanabe, J. Appl. Phys. 45 (2006) L963.

[70] B. W. Smith and D. E. Luzzi, J. Appl. Phys. 90 (2001) 3509.

[71] A. V. Krasheninnikov and K. Nordlund, Nucl. Instrum. Methods Phys. Res. B 216 (2004) 355.

[72] J. Kotakoski, A. V. Krasheninnikov, Y. Ma, A. S. Foster, K. Nordlund, and R. M. Nieminen, Phys. Rev. B 71 (2005) 205408.

[73] A. V. Krasheninnikov, K. Nordlund, and J. Keinonen, Phys. Rev. B 65 (2002) 165423.

[74] J. A. V. Pomoell, A. V. Krasheninnikov, K. Nordlund, J. Keinonen, J. Appl. Phys. 96 (2004) 2864.

[75] B. Q. Wei, J. D'Arcy-Gall, P. M. Ajayan, and G. Ramanath, Appl. Phys. Lett. 83 (2003) 3581.

[76] Y. Zhu, T. Yi, B. Zheng, and L. Cao, Appl. Surf. Sci. 137 (1999) 83.

[77] P. Vincent, A. Brioude, C. Journet, S. Rabaste, S. T. Purcell, J. L. Brusq, and J. C. Plenet, J. Non-Cryst. Solids 311 (2002) 130.

[78] F. Banhart, Rep. Prog. Phys. 62 (1999) 1181.

[79] M. Terrones, H. Terrones, F. Banhart, J.-C. Charlier, P. Ajayan, Science 288 (2000) 1226.

[80] P. M. Ajayan, V. Ravikumar, and J.-C. Charlier, Phys. Rev. Lett. 81 (1998) 1437.

[81] W. E. Gettys, Physical Rev. 146 (1996) 480.

[82] P. Vajda, Rev. Mod. Phys. 49 (1977) 481.

[83] N. G. Ghopra, F. M. Ross and A. Zettl, Chem. Phys. Lett. 256 (1996) 241.

[84] D. Ugarte, Nature 354 (1991) 56.

[85] D. Ugarte, Chem. Phys. Lett. 207 (1993) 473.

[86] J.F. Ziegler, J.P. Biersack, M.D. Ziegler, <http://www.srim.org>.

[87] A. Aitkaliyeva, L. Peng, D. Saenz, M. Martin, D. Wijesundera, X. Wang, W.-K. Chu, and Lin Shao, AIP Conference Proceedings Vol. 1099 (2009) 393.

[88] F. Tuinstra and J.L. Koenig, J. Chem. Phys. 53 (1970) 1126.

[89] V. Skákalová, J. Maultzsch, Z. Osváth, L. P. Biró, and S. Roth, Phys. State. Sol. (1) 4 (2007) 138.

[90] G. Compagnini, G. A. Baratta, R.S. Cataliotti, and A. Morresi, J. Raman Spectrosc. 26 (2005) 917.

[91] T. Tanabe, Phys. Scr. T 64 (1996) 7.

[92] K. Niwase, Phys. Rev. B 52 (1995) 15785.

[93] K. Nakamura and M. Kitajima, Phys. Rev. B 45 (1992) 78.

[94] K. Niwase, T. Tanabe, and I. Tanaka, J. Nucl. Mater. 191 (1992) 335.

[95] J. Seldin and C.W. Nezbeda, J. Appl. Phys. 41 (1970) 3389.

[96] E. Salonen, A. V. Krasheninnikov, and K. Nordlund, Nucl. Instrum. Methods Phys. Res. B 193 (2002) 603.

[97] Z. H. Xia, P.R. Guduru, and W.A. Curtin, Phys. Rev. Lett. 98 (2007) 245501.

[98]   A. V. Krasheninnikov, K. Nordlund, P.O. Lehtinen, A.S. Foster, A. Ayuela, and R.M. Nieminen, Phys. Rev. B 69 (2004), 073402.

[99]   V. A. Basiuk, K. Kobayshi, T. Kaneko, Y. Negishi, E. V. Basiuk, J.-M. Saniger-Blesa, Nano Lett. 2 (2002) 789.

[100] B. Khare, M. Meyyappan, M. H. Moore, P. Wilhite, H. Imanaka, B. Chen, Nano Lett. 3 (2003) 643.

[101] T. Belin, F. Epron, Mater. Sci. Eng. B. 119 (2005) 105.

[102] S. Mathew, U. M. Nhatta, J. Ghatak, B. R. Sekhar, B. N. Dev, Carbon 45 (2007) 2659.

[103] A. R. Adhikari, M. B. Huang, H. Bakhru, S. Talapatra, P. M. Ajayan, C. Y. Ryu, Nucl. Instrum. Methods Phys. Res. B 245 (2006) 431.

VITA

Assel Aitkaliyeva was born in Almaty, Kazakhstan on January 12, 1985. She started college in 2002 at al-Farabi Kazakh State University. She graduated with a Bachelor of Science degree in physics in June of 2006. She entered the Nuclear Engineering program at Texas A&M University in September 2007 and received her Master of Science degree in August 2009. Her research interests include irradiation stability of various materials at a nanoscale. She can be contacted through the Department of Nuclear Engineering, Texas A&M University, College Station, Texas 77843-3133.